Working Principle of a Li_2CO_3/$LiNbO_3$ Coating on NCM for Thiophosphate-based All-Solid-State Batteries

Felix Walther [a,b], Florian Strauss [c], Xiaohan Wu [d], Boris Mogwitz [a,b],
Jonas Hertle [a,b], Joachim Sann [a,b], Marcus Rohnke [a,b], Torsten Brezesinski [c]
and Jürgen Janek [a,b,c,*]

[a]*Institute of Physical Chemistry, Justus Liebig University Giessen, Heinrich-Buff-Ring 17, D-35392 Giessen, Germany.*

[b]*Center for Materials Research (LaMa), Justus Liebig University Giessen, Heinrich-Buff-Ring 16, D-35392 Giessen, Germany.*

[c]*Battery and Electrochemistry Laboratory, Institute of Nanotechnology, Karlsruhe Institute of Technology (KIT), Hermann-von-Helmholtz-Platz 1, D-76344 Eggenstein-Leopoldshafen, Germany.*

[d]*BASF SE, Carl-Bosch-Str. 38, D-67056 Ludwigshafen am Rhein, Germany.*

*E-mail: juergen.janek@phys.chemie.uni-giessen.de

Abstract

Large-scale industrial application of all-solid-state-batteries (ASSBs) is currently hindered by numerous problems. Regarding thiophosphate-based ASSBs, interfacial reactions with the solid electrolyte are considered a major reason for capacity fading. On the positive electrode side, cathode active material coating addresses these issues and improves the ASSB performance. Yet the working principle of the coating often remains unclear, and protection concepts on the way to long-term stable ASSBs remain empirical. In this work, we characterize the influence of a $Li_2CO_3/LiNbO_3$ cathode active material coating on the battery performance and cathode degradation reactions of a $Li_4Ti_5O_{12}$/Super C65 | Li_6PS_5Cl | $LiNi_{0.6}Co_{0.2}Mn_{0.2}O_2$/$Li_6PS_5Cl$/Super C65 cell. The coating microstructure is characterized comprehensively using a combination of focused ion beam scanning electron microscopy (FIB-SEM), X-ray photoelectron spectroscopy (XPS) and time-of-flight secondary ion mass spectrometry (ToF-SIMS). Based on this knowledge, we demonstrate and discuss the positive effect of the coating on the ASSB performance. Finally, we present an in-depth post-mortem analysis of composite cathodes by combining XPS depth profiling with ToF-SIMS. The $Li_2CO_3/LiNbO_3$ coating suppresses the interfacial reaction at the cathode active material/solid electrolyte interface, in particular the formation of oxygenated phosphorous and sulfur compounds such as phosphates and sulfates/sulfites, leading to a significantly enhanced ASSB performance.

Introduction

All-solid-state batteries (ASSBs) are one of the most promising candidates for future energy storage devices.[1–5] They are considered to have many advantages over conventional energy storage systems. First, ASSBs may enable the use of lithium metal as anode material, which could lead to energy storage devices with higher specific energies compared to conventional lithium-ion batteries (LIBs) based on liquid electrolytes.[6] Second, the cell design can be simplified, which enables the possibility of roll-to-roll cell production.[7] The latter is mandatory for large-scale applications to make ASSBs economically more attractive. Third, the replacement of the flammable organic liquid electrolyte in LIBs can enhance safety, which makes ASSBs particularly attractive for the automotive sector, since safety is one of the most important arguments for marketing.[8,9]

Several classes of solid electrolytes can be distinguished and have already been tested for use in ASSBs.[10] Thiophosphates are considered as one the most promising candidates, since they provide high ionic conductivities and can be processed readily due to their malleability.[11] However, problems which are often associated with the stability of these materials must be addressed and solved to enable the transfer from research status to large-scale application.[12,13]

Research efforts are currently ongoing in various fields to overcome problems related to ASSBs. Simulations deal with the detection of critical parameters for cell performance and the optimization of cell design.[14–18] In the field of materials synthesis, novel anode/cathode materials and new solid electrolytes are being developed.[19,20] In addition, much research is done to clarify degradation phenomena and develop strategies to prevent them. With regard to thiophosphate-based composite cathode, this mainly includes doping approaches of the solid electrolyte and the development of protective coatings for cathode active materials (CAM).[21–23] According to literature, the latter strategy seems promising to address interfacial issues and to enhance the ASSB performance. However, the working principle of the CAM modification often remains unclear.[21] From an analytical point of view, two main reasons can be derived:

i) *Insufficient characterization of the coating.*

Knowledge about coating morphology and composition is needed to obtain a comprehensive picture of the microstructure. This in turn is mandatory to discuss the coating influence on the ASSB performance and the corresponding decomposition processes. However, the characterization of the coating microstructure is highly challenging due to the small dimensions of thin coatings (in the nm range) and the low material concentrations. Basically, a wide variety of analytical methods can be used to solve this task, but there is no analytical tool that can provide all the necessary information at once. Microscopic methods such as scanning electron microscopy (SEM) and transmission electron microscopy (TEM), for example, offer a very high spatial resolution, but cannot intrinsically provide detailed information on the chemical composition. In contrast, spectroscopic methods such as X-ray photoelectron spectroscopy (XPS) and energy-dispersive X-ray spectroscopy (EDX) can provide detailed information on the

chemical composition, but suffer from relatively poor spatial resolution. Therefore, a combination of several methods is mandatory. When selecting the methods, it is important to know the respective method-specific limits in order to compensate for them. Accordingly, a coating characterization by global investigations such as top-view SEM for morphological information and EDX for chemical information, for example, are not sufficient to comprehensively characterize the coating, since only rough conclusions on morphological changes and the element distribution on the CAM particles are possible. In contrast, information on the spatially resolved coating microstructure (morphology and chemical composition) cannot be obtained in this way. Consequently, the effect of the coating on the battery performance is difficult to interpret and the reasons for the often-remaining capacity fade during battery cycling remain elusive.

ii)   Insufficient separation of the individual degradation processes in the composite cathode.

The post-mortem analysis of composite cathodes is often insufficient to separate the individual decomposition contributions. Accordingly, it is often not clear on which part of the degradation in the composite cathode the coating has an influence. Walther *et al.* have very recently shown that global (i.e. integral) measurements on the (uncleaned) cathode surface make an interpretation of the results extremely difficult due to spatially convoluted decomposition processes, which in turn does not allow any conclusions to be drawn on the individual decomposition contributions.[24] As a result, the protective effect of a coating is often generally related to the suppression of battery degradation processes (unspecific statements) or, what is basically worse, wrong conclusions are drawn due to the overlap of one or more degradation processes that occur in different areas of the cathode composite.

In this work, we investigate a $Li_2CO_3/LiNbO_3$ coating on $LiNi_{0.6}Co_{0.2}Mn_{0.2}O_2$ (NCM622). A $LiNbO_3$-based coating has been chosen, since it is a well-established material for protective coatings in ASSBs and its positive effect on the battery performance has been widely demonstrated in literature.[21,25–27] We have combined $LiNbO_3$ with Li_2CO_3, as Li_2CO_3 is reported to be potentially beneficial for ternary lithium metal oxide coatings.[26,28] In addition, Ni-rich NCM materials are known to form carbonates on the surface depending on storage conditions and aging effects.[29,30] Therefore, we assume that the presence of Li_2CO_3 is inherently relevant when it comes to the interface reaction between the CAM and the solid electrolyte. For these reasons we have intentionally introduced Li_2CO_3 to the coating.

Although $LiNbO_3$-based coatings are well-established for ASSBs, the protective mechanism, however, is still not yet fully understood. Thus, the aim of this work is to gain detailed insights into the working principle of such a protective coating. The focus of the study is on its influence on the interfacial decomposition processes between the CAM and the thiophosphate-based solid electrolyte.

First, we characterize the microstructure of the coating which includes the morphology and the chemical composition. In general, TEM is a highly suitable technique for this task, especially in combination with EDX and/or electron energy loss spectroscopy (EELS). However, the sample preparation requires a

relatively high effort and TEM investigations involve the risk of decomposition of radiation-sensitive compounds, like e.g. Li_2CO_3, which can only be partially compensated by measuring under cryogenic conditions. In addition, the results obtained are locally restricted to a relatively small analysis area, making it difficult to draw more general conclusions, e.g. on the overall coating coverage. Kim *et al.* already used the combination of TEM, EDX and EELS to characterize the coating microstructure of a Li_2CO_3/$LiNbO_3$ hybrid coating.[26] Since the information obtained was limited to basic statements such as the local coating thickness and the element distribution, the authors had to apply additional techniques to get further insights into the coating composition. Therefore, we develop here a different approach to gain a comprehensive picture of the coating microstructure. The characterization is mainly achieved by using a combination of focused ion beam scanning electron microscopy (FIB-SEM), X-ray photoelectron spectroscopy (XPS) and time-of-flight secondary ion mass spectrometry (ToF-SIMS). With this approach, we show that the coating is particulate and homogeneously distributed over the NCM622 secondary particle structure. In addition, we reveal its chemical composition and finally clarify the coating microstructure. Second, we demonstrate the positive influence of the Li_2CO_3/$LiNbO_3$ coating on the cycling performance of a $Li_4Ti_5O_{12}$/Super C65 | Li_6PS_5Cl | NCM622/Li_6PS_5Cl/Super C65 cell. Third, a comprehensive post-mortem analysis is performed to characterize the influence of the CAM coating on the decomposition processes in the composite cathode using XPS and ToF-SIMS. We show that the CAM coating suppresses the interfacial reaction at the NCM622/solid electrolyte interface mainly in terms of phosphate and sulfate/sulfite formation. However, because it cannot be completely prevented, we still expect capacity fading due to reactions occurring at the CAM/solid electrolyte interface.

Overall, we demonstrate that ToF-SIMS in particular is very powerful to determine the influence of coatings on the interfacial decomposition processes and seems suited for benchmarking the effectiveness of protective CAM coatings in such composite cathodes on a semi-quantitative basis.

Experimental Section

Preparation of ASSB Cells.

Materials.

NCM622 (d_{50} = 2.9 µm and d_{90} = 6.0 µm) powder (BASF SE) and Super C65 carbon black (Timcal) were dried for 12 h in vacuum at 300 °C and then stored in an argon-filled glovebox (< 0.1 ppm O_2, < 0.1 ppm H_2O).[31] Li_6PS_5Cl solid electrolyte was prepared by milling 5 g of a stoichiometric mixture of a Li_2S (10 mol % deficiency), P_2S_5 and LiCl (Alfa Aesar; 99+%) under argon atmosphere for 1 h at 250 rpm first and then for 20 h at 450 rpm using a 250 mL zirconia jar containing 10 mm zirconia balls with a 30:1 ball-to-powder ratio. LiCl was dried in vacuum (~10^{-3} mbar) for ~12 h at 300 °C prior to usage. After milling, the powder was annealed in vacuum (~10^{-3} mbar) for 5 h at 300 °C. The room-temperature ionic conductivity of the resulting Li_6PS_5Cl solid electrolyte was ~2.0 mS/cm. Further details such as X-ray diffraction patterns can be found in a previous work.[32]

Coating approach.

The Li_2CO_3/$LiNbO_3$ coating was applied to the NCM622 according to a procedure published in literature.[25,26] 1M lithium ethoxide solution was prepared by reacting absolute ethanol (Sigma-Aldrich; 99.8%) and Li metal (Albemarle Germany GmbH). For 0.5M niobium ethoxide solution, $Nb(OCH_2CH_3)_5$ (Sigma-Aldrich; 99.95%) was dissolved in absolute ethanol. Note that the Li to Nb molar ratio was 2 to 1. The obtained powder was subsequent heated in air at 300 °C for 2 h (5 °C/min heating rate) and stored under argon atmosphere for further use.

A coating reference was prepared analogously on a silicon wafer. The Li metal supplier for this sample was abcr GmbH. In this case, the Li to Nb molar ratio was 1 to 1 (for the stoichiometry $LiNbO_3$).

Material characterization.

Scanning electron microscopy (SEM) was performed using a LEO-1530 microscope (Carl Zeiss AG) to characterize the cathode active material in terms of particle size distribution and basic morphology (see Supporting Information Figure S1).

Attenuated total reflection-infrared spectroscopy (ATR-IR) was performed using an ALPHA FT-IR spectrometer (Bruker Corporation) equipped with a Ge crystal in an argon filled glovebox to confirm the presence of Li_2CO_3 in the coating material (see Supporting Information Figure S2). The spectra were collected using the OPUS software.

Preparation of Electrode Composites.

The cathode composite powder was prepared by milling NCM622, Li_6PS_5Cl and Super C65 carbon black (1 g, 7/3/0.1 weight ratio) using ten 10 mm zirconia balls in a planetary mill at 140 rpm for 30 min under argon atmosphere. The anode composite powder was a 3/6/1 weight ratio mixture of carbon-

coated $Li_4Ti_5O_{12}$ (NEI Corporation; LTO), Li_6PS_5Cl and Super C65 carbon black and was prepared in the same way as the cathode composite.

Cell Assembly and Electrochemical Characterization.

For pelletized ASSB test cells (Ø 10 mm), a custom setup comprising two stainless steel dies and 10 mm diameter PEEK sleeve was used. In the assembling procedure, Li_6PS_5Cl (100 mg) was compressed at 125 MPa. Afterward, the anode composite (65 mg) was pressed to the solid electrolyte pellet at 125 MPa (~120 µm thickness) and finally the cathode composite (10-12 mg) was pressed onto the other side at 375 MPa. A pressure of 55 MPa was maintained upon electrochemical testing. Galvanostatic measurements were performed at C/5 rate (1C = 180 mA·g^{-1}) and 45 °C in the voltage range between 1.35 and 2.85 V vs. $Li_4Ti_5O_{12}/Li_7Ti_5O_{12}$ using a MACCOR battery test system.

Sample Handling and Sample Transfer.

All samples were prepared at the Battery and Electrochemistry Laboratory, Karlsruhe Institute of Technology (KIT) (Eggenstein-Leopoldshafen, Germany). The chemicals were stored and handled in an argon-filled glovebox (< 0.1 ppm O_2, < 0.1 ppm H_2O). For analysis, the samples were sealed in pouches under argon atmosphere and shipped to the Institute of Physical Chemistry, Justus Liebig University Giessen (Giessen, Germany). The samples were stored and prepared for analyses in an argon-filled glovebox again (< 0.1 ppm O_2, < 0.1 ppm H_2O). The sample transfer into the instruments was realized by using two different transfer systems. For FIB-SEM and ToF-SIMS analyses, the transfer system Leica EM VCT500 (Leica Microsystems GmbH) was used. For XPS analyses, all samples were transferred under argon atmosphere from the glovebox into the instrument by using a transport box for PTS sample holders by PREVAC.

Focused Ion Beam Scanning Electron Microscopy (FIB-SEM).

The cross-sections in this work were created and analyzed with a TESCAN XEIA3 system (TESCAN GmbH) equipped with a Xe plasma FIB column. The CAM particles were attached to conductive double-sided adhesive carbon-tabs. For charge compensation, the samples were previously (non-conformally) coated with Pt using a Leica EM ACE600 high vacuum sputter coater (Leica Microsystems GmbH). Typically, a layer thickness of 4 nm was used. Cross-sections were carried out on clusters of secondary particles. Then, the inner secondary particles were analyzed to exclude detrimental effects of the Pt layer. Accordingly, geometrical shadowing effects due to the directional sputtering flux were exploited and all measurements were double checked to ensure the reliability of the results. In all experiments, the Xe ion beam energy was 30 kV. The beam current was 130 nA for milling and 8 nA for polishing.

Time-of-Flight Secondary Ion Mass Spectrometry (ToF-SIMS).

ToF-SIMS analysis was performed by using a TOF.SIMS 5-100 system (IONTOF GmbH). The system is equipped with a 25 keV Bi cluster primary ion gun for analysis and dual-source column, which enables depth profiling by using either O_2^+ or Cs^+ (up to 2 keV). In addition, a focused ion beam (FIB) option can be used to mill craters with monatomic gallium (30 keV).

The samples were attached to the sample holder using non-conductive adhesive tape. The surface of the samples was flooded with low-energy electrons for charge compensation. All measurements in this work were performed in negative ion mode using Bi_3^+ species (25 keV) for analysis and a cycle time of 60 µs.

Surface analysis was performed by operating the instrument in spectrometry mode (bunched mode). This mode enables high signal intensities and a high mass resolution [FWHM $m/\Delta m > 4500$ @ $m/z =$ 31.97 (S^-)] which minimizes the effects of signal interferences in the mass spectra. The analysis area was set to (150×150) µm² and rasterized with (256×256) pixels. Every patch was analyzed with 1 frame and 1 shot per pixel and frame. For comparable measuring conditions, the analyses were stopped after a primary ion dose of $1.00 \cdot 10^{12}$ ions/cm² (static conditions). The primary ion current was about 0.5 pA. We measured ten mass spectra per sample in different areas on the sample surface to minimize area dependent effects and to ensure the reproducibility of results.

To investigate the bulk material, ToF-SIMS analysis was carried out on 45° FIB crater sidewalls. The (120×80) µm² craters were milled with (512×512) pixels (FoV: (150×150) µm²) into the composite cathodes by using the FIB option of the instrument, allowing subsequent analysis of the crater sidewalls without additional transfer steps. A 700 µm aperture was used and the dwell time was 200 ms per pixel. The FIB current was about 16-17 nA (100% duty cycle). The analysis of the crater sidewall was performed by operating the instrument in fast imaging mode. The primary ion current was about 0.2 pA. A region-of-interest (ROI) was defined within a (125×125) µm² analysis area to analyze only the crater sidewall. Before analysis, the damage layer on top of the crater sidewall caused by the FIB was removed by a cleaning procedure analogous to our previous work.[33] The subsequent analysis of the crater sidewall was performed with a raster size of (1024×1024) pixels at 1 shot per pixel and 50 frames. This corresponds theoretically to a maximum lateral resolution of 122 nm. However, this value should be seen as the maximum resolution under ideal conditions, since topographic effects and the inclined position of the crater have a non-negligible negative influence.

The analysis of the $LiNbO_3$ reference on a silicon wafer was performed by operating the instrument in fast imaging mode. The analysis current was ~0.2 pA. The analysis area was (200×200) µm² and rasterized with (512×512) pixels. Every patch was analyzed with 10 frames, whereas 1 shot per pixel and frame was used. Depth profiling was performed in non-interlaced mode with Cs^+ (2 keV) as sputter species. The sputter current was ~136 nA. The crater size was set to (500×500) µm² and sputtered with 600 frames followed by a pause of 1.0 s.

The evaluation of ToF-SIMS data was done with the software SurfaceLab 7.0 (IONTOF GmbH). All secondary ion images in this work were normalized in relation to the total ion signal to minimize topographic effects. The signal intensities were extracted from the respective normalized secondary ion images.

X-ray Photoelectron Spectroscopy (XPS).

XPS analyses was carried out by using a PHI5000 Versa Probe II system (Physical Electronics GmbH). The samples were attached to the sample holder using non-conductive adhesive tape. A dual beam charge neutralization (ion beam combined with a low-energy electron beam) was applied during the measurements. Depth profiling was performed analogous to our previous work to clean the surface of the composite cathode in order to minimize the detrimental influence of the degradation processes at the current collector/solid electrolyte interface.[24,33] The change of signals was monitored as a function of the sputtering time for all samples to minimize the influence of the current collector/solid electrolyte interface on the one hand and to exclude further sample modification by sputtering on the other hand. For comparison of XP spectra, a Li_6PS_5Cl reference (NEI Corporation) was used.

For analysis, monochromatic Al Kα radiation (1486.6 eV) was used. The X-ray source was operated with a power of 50 W and a voltage between 15-17 kV. The analysis beam diameter was 200 μm. The pass energies of the analyzer ranged from 23.50 eV to 46.95 eV. The exact values are given in the respective captions of the XP spectra.

The depth profiling experiments were performed in alternating sputter mode. For material abrasion, a sputter gun with Ar^+ ions was used. The acceleration voltage was set to 0.5 kV with a sputter current of ~0.5 μA. The raster size was (2×2) mm^2.

The experimental data was evaluated with the software CasaXPS (version 2.3.22, Casa Software Ltd). The energy calibration was performed analogous to previous work to minimize detrimental surface effects.[34,35] Accordingly, the XP spectra of the Li_6PS_5Cl reference were calibrated in relation to the signal of adventitious carbon at 284.8 eV first. Afterwards, the energetic signal position of the main component of the S 2p signal (PS_4^{3-} units) was determined and the XP spectra of the composite cathodes were calibrated in relation to this signal at 161.6 eV. The suitability of the energy calibration was double checked with other main components of the solid electrolyte. For signal fitting, Shirley background, GL(30) line shapes and common fitting restrictions were used. The latter include theoretical signal area ratios dependent on the analyzed orbital (e.g. 1:2 for p orbitals), FWHM constraints and published values for spin orbit splitting.[36]

Results

The results section of this work is divided into three parts. First, we characterize the microstructure of the Li_2CO_3/$LiNbO_3$ coating, namely the morphology and composition. In the second part, we address the influence of the CAM coating on the ASSB performance and demonstrate its beneficial effect. In the third part, we present a comprehensive post-mortem analysis of composite cathodes by XPS and ToF-SIMS measurements to clarify the working principle of the Li_2CO_3/$LiNbO_3$ coating.

Characterization of the Coating Microstructure.

For thorough characterization of the coating microstructure, it is necessary to address the coating morphology as well as the coating composition. In this work, we used FIB-SEM to characterize the coating morphology, followed by the characterization of the coating composition using XPS and ToF-SIMS.

The difference in the atomic mass of Nb compared to the elements of NCM allows for sufficient material contrast in SEM micrographs measured using a back scattered electron (BSE) detector to distinguish the CAM coating from the NCM material. Figure 1 shows representative SEM images, revealing the morphology of the Li_2CO_3/$LiNbO_3$ coating and its distribution on the CAM surface.
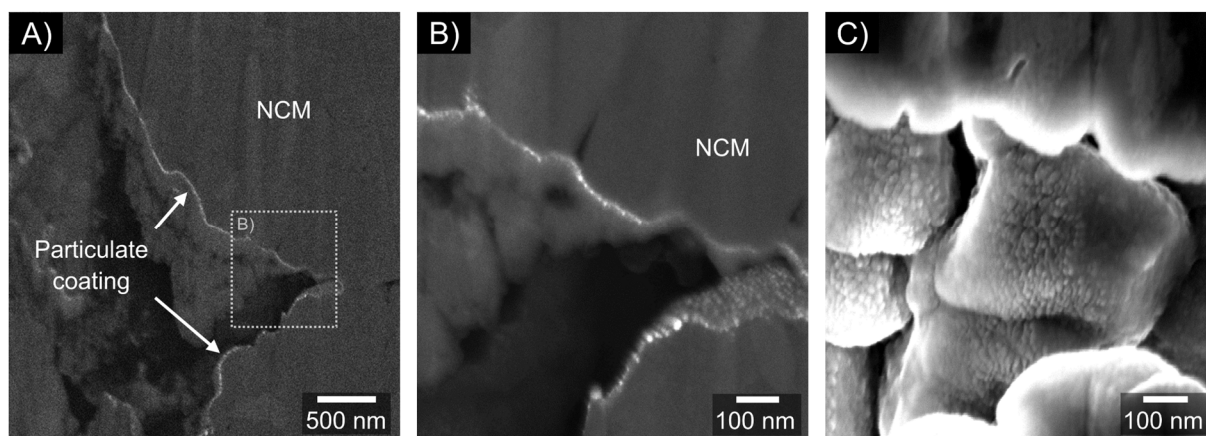
Figure 1. FIB-SEM micrographs of the Li_2CO_3/$LiNbO_3$ coated NCM622 particles. (A) Cross-sections of coated NCM622 particles. (B) Magnified SEM image. (C) Top-view on the secondary particle surface. The images were obtained by using a BSE detector, allowing for sufficient material contrast to distinguish the coating from the NCM. The images reveal a particulate coating (mean thickness ~15 nm) with a high particle density. The coating particles are homogeneously distributed on the NCM622 particle surface; however, some uncoated areas are visible.

The SEM micrographs reveal a particulate coating with a mean thickness of about 15 nm. The coating particles are homogenously distributed on the NCM622 particle surface, leading to a high degree of coverage. However, the particular character still allows open (uncoated) areas between the particles, which will be particularly important later on in the context of decomposition phenomena in the composite cathodes. Accordingly, we still expect decomposition reactions to occur in the uncoated/less-coated

10

areas. However, the SEM analyses reveal a high quality of the coating in terms of homogeneity, meaning that variations of coating particle size/thickness are comparably small. These are ideal conditions for the post-mortem analysis on composite cathodes shown later, since no significant dependence on the analysis area is to be expected.

To characterize the coating composition, we performed XPS and ToF-SIMS analyses. XPS is used for basic statements on the material composition, which is complemented by ToF-SIMS for characterizing the locally resolved material distribution. Figure 2A shows a comparison of the XP detail spectra of the coated CAM with two reference samples. For the coated CAM (Figure 2A top), the energetic signal position of contributions in the Nb 3d and the O 1s spectra agree well with literature values for $LiNbO_3$.[37,38] In addition, contributions which can be assigned to Li_2CO_3 are visible in the C 1s and O 1s spectra.[39] ATR-IR measurements (see Supporting Information Figure S2) and a comparison of the energetic XP signal positions with a Li_2CO_3 coated NCM622 reference further verify the presence of Li_2CO_3.[26] Apart from both the $LiNbO_3$ and Li_2CO_3, contributions from aliphatic carbon can be observed in the C 1s signal and an additional signal caused by NCM622 is visible in the O 1s spectrum for the coated particles.[40,41] The latter is not very surprising for the coated CAM considering the particulate nature of the coating.

To get more information about the microstructure of the coating, we prepared a model sample by coating a silicon wafer (see Experimental Section) followed by ToF-SIMS analysis. The flat geometry of the silicon wafer allows a reliable characterization of the microstructure using ToF-SIMS. Depth profiling in fast imaging mode was performed to enable a 3D reconstruction of the coating particles with a high spatial resolution and simultaneously chemical information. The suitability of the selected signals for the 3D reconstruction was verified by measurements performed in spectrometry mode (bunched mode), offering a higher mass resolution. Figure 2B shows the obtained 3D reconstructions. It can be seen that large particles were grown on the silicon substrate. The particle dimensions are much larger compared to the coating of the NCM622 particles, which is most likely related to the greater amount of material used and the substrate itself. Besides the changed surface composition, the reduced surface roughness in case of the silicon wafer can also have an influence on the nucleation and the subsequent material growth process. However, the XPS results (Figure 2A middle) show similar chemical components, demonstrating the suitability of the model sample. Taking these considerations into account, several conclusions can be drawn from the model sample:

The inner region of the coating particles shows fragments which can be related to $LiNbO_3$ (green). The $LiNbO_3$ is most probably present as amorphous phase, since the heating temperature was only 300 °C. For comparison, Glass *et al.* reported an initial crystallization temperature of 460 °C for $LiNbO_3$, whereas Özer and Lampert observed crystallization not before 550 °C for a synthesis route similar to this work.[42,43] Carbonate fragments originate from the surface of the particles (yellow), whereas C⁻ fragments are formed from regions between the particles (red). Based on the XPS results, we assume that

the carbonate fragments are formed from Li_2CO_3. C^- is most probably related to ethoxide residues and related side products from the coating process. This could also explain the relative high signal intensity of corresponding contributions in the binding energy range of aliphatic carbon in the C 1s spectrum.
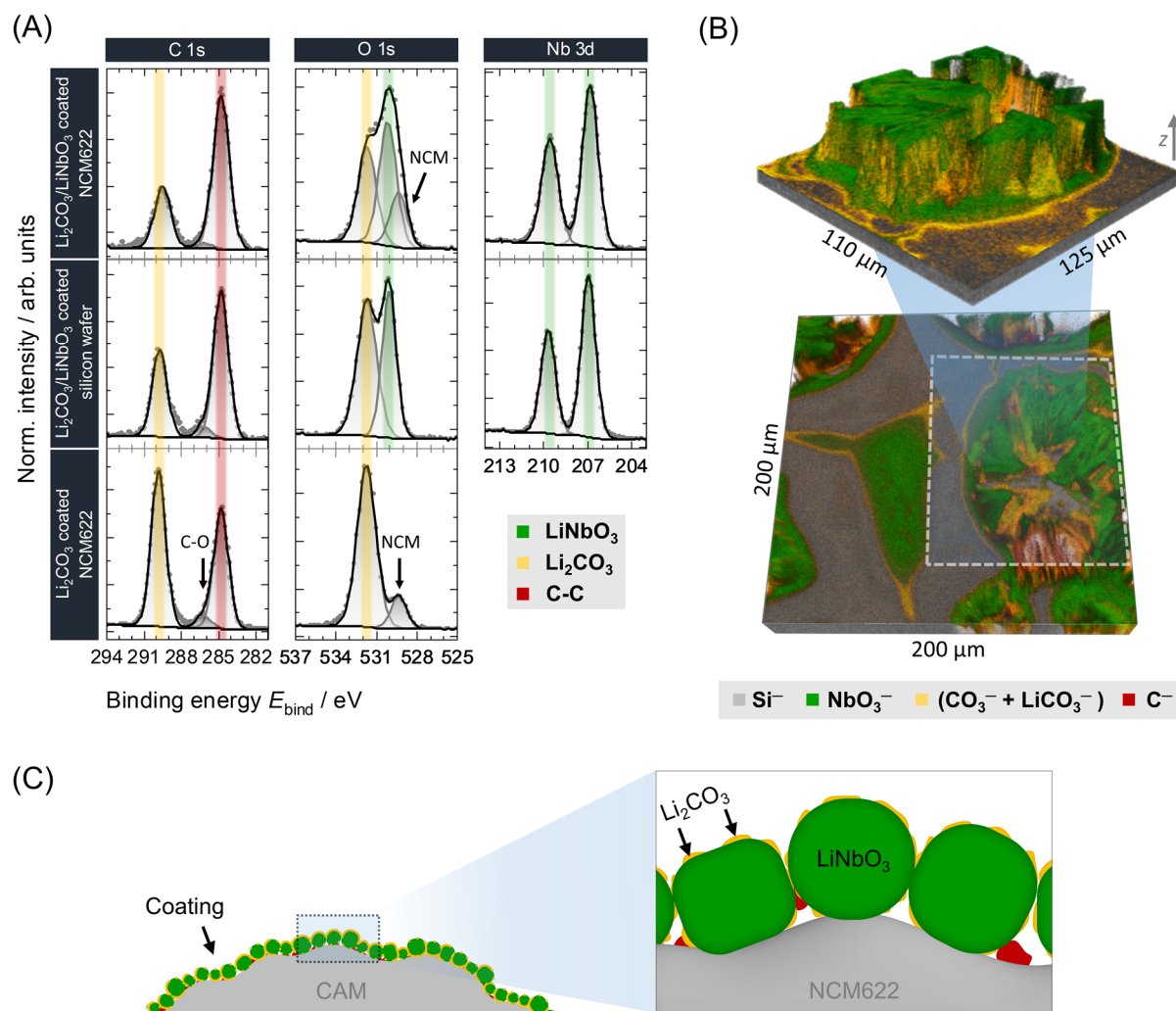
Figure 2. (A) XP detail spectra of the $Li_2CO_3/LiNbO_3$ coated NCM622 particles. Reference spectra of a $Li_2CO_3/LiNbO_3$ coated silicon wafer (model sample) and Li_2CO_3 coated NCM622 particles are shown for comparison. All spectra were measured using a pass energy of 23.50 eV. The energetic signal positions agree with literature values for $LiNbO_3$, Li_2CO_3 and NCM.[37–41] In addition, contributions in the C 1s spectrum caused by ethoxide residues and related side products seem reasonable. (B) ToF-SIMS 3D reconstruction of a $Li_2CO_3/LiNbO_3$ coated silicon wafer (model sample) to clarify the microstructure of the coating particles. The upper image was obtained by using a 3D correction. (C) Proposed microstructure for the $Li_2CO_3/LiNbO_3$ coating. Accordingly, the coating is particulate with a mean particle size in the range of ~15 nm. The inner part of the particles consists of $LiNbO_3$, surrounded by a Li_2CO_3 containing shell. In between, ethoxide residues from the synthesis process may be expected.

Overall, taking the FIB-SEM, XPS and ToF-SIMS results into account, we propose the coating micro-structure shown in Figure 2C, which can be described as follows: The coating is particulate with a mean particle size in the range of ~15 nm and consists of an amorphous $LiNbO_3$ core and a Li_2CO_3 containing shell. In between the particles, ethoxide residues and related side products from the synthesis process are conceivable.

In this context, it must be noted that small stoichiometric deviations from the postulated stoichiometry cannot be detected by XPS and ToF-SIMS. Calculations by Xiao *et al*. suggest that at the NCM (fully-lithiated)/$LiNbO_3$ interface compounds such as Li_3NbO_4 can be formed.[44] We assume that it is almost impossible to distinguish such (partial) stoichiometric deviations due to small binding energy shifts in XP spectra and similar fragmentations in ToF-SIMS spectra. In addition, small concentrations are generally problematic taking the respective detection limit of the analytical methods into account. However, it should be noted that according to the aforementioned calculations, the reaction energy and thus the driving force for the reaction is very small. Calculations of Nolan *et al*. further support that the driving force for the reaction of $LiNbO_3$ with fully-lithiated nickel-rich CAMs is low.[45] Therefore, based on our analytical results and the calculations mentioned, we will use the simplified term Li_2CO_3/$LiNbO_3$ coating in the following.

Electrochemical Cell Performance.

To investigate the effect of the Li_2CO_3/$LiNbO_3$ coating on the ASSB long-term cycling performance, pelletized bulk-type cells were assembled and charged/discharged for 200 cycles. For comparison, similar cells comprising bare (uncoated) NCM622 were also tested. Initial specific charge and discharge capacities of 188 $mAh \cdot g^{-1}$ and 161 $mAh \cdot g^{-1}$ were achieved for the bare NCM622, corresponding to a Coulomb efficiency (CE) of 86% (Figure 3A top). With subsequent cycling, fast capacity fading can be observed, reaching specific discharge capacities of 86 $mAh \cdot g^{-1}$ and 22 $mAh \cdot g^{-1}$ at the 50th and 200th cycle, respectively. For the Li_2CO_3/$LiNbO_3$ coated NCM622, initial specific charge and discharge capacities of 200 $mAh \cdot g^{-1}$ and 180 $mAh \cdot g^{-1}$ were achieved with a CE of 90% (Figure 3A bottom). It can therefore be stated that the CAM coating leads to an improvement in the initial CE of 4%, together with an increased absolute charge/discharge capacity. With subsequent battery cycling, a steady but much less pronounced specific discharge capacity decay is apparent for the coated sample (Figure 3B), reaching 153 $mAh \cdot g^{-1}$ and 82 $mAh \cdot g^{-1}$ for the 50th and 200th cycle, respectively. Regarding the CE, both CAMs (coated and uncoated) approach 99.5% after around 38 cycles. However, the CEs for the bare NCM622 are roughly 0.5% lower than for the coated NCM622 in the following cycles (see Supporting Information Figure S3), indicating more pronounced interfacial side reactions.

13
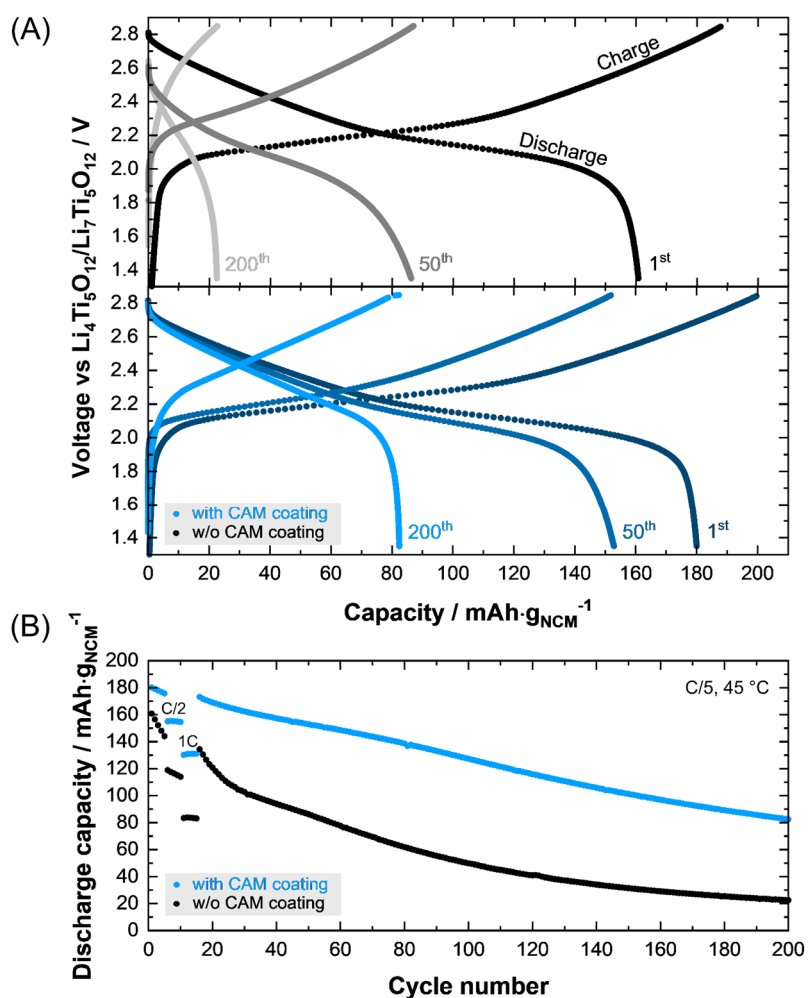
Figure 3. (A) Charge and discharge curves for bare (top) and $Li_2CO_3/LiNbO_3$ coated NCM622 (bottom) for the initial, 50th and 200th cycles. (B) Long-term cycling performance in terms of specific discharge capacities as a function of cycle number. The corresponding Coulomb efficiencies are shown in the Supporting Information. Application of the CAM coating leads to an enhanced ASSB performance, thus demonstrating its overall beneficial effect.

Post-Mortem Analysis.

In this chapter, we show the results of post-mortem analysis using XPS and ToF-SIMS for composite cathodes with bare and $Li_2CO_3/LiNbO_3$ coated NCM622. The aim was to obtain a comprehensive picture on the influence of the coating on the decomposition reactions in the composite cathode. In the following, the results are addressed separately in two parts according to the respective analytical method.

I) X-Ray Photoelectron Spectroscopy.

XPS depth profiling experiments were conducted to identify decomposition products and to draw quantitative conclusions. Analogous to our previous work, the surface of the composite cathodes was initially cleaned by Ar^+ sputtering to reduce the detrimental effect of the current collector (see Experimental Section).[24] To characterize the influence of the CAM coating on the decomposition processes, we conducted analysis on composite cathodes with bare and coated NCM622 after 0 cycles (as-prepared) and

14

200 cycles. The S 2p and P 2p spectra will be used hereafter to discuss basic decomposition processes indicated by XPS (Figure 4A). Then, we address the signal changes in the Nb 3d spectrum as a function of different cycling stages (Figure 4B). The Cl 2p, O 1s, Li 1s and C 1s detail spectra are shown in the Supporting Information (Figure S4).

Figure 4A shows a direct comparison of the S 2p and P 2p detail spectra before and after battery cycling for $Li_2CO_3/LiNbO_3$ coated and bare NCM622. Reference spectra for the Li_6PS_5Cl solid electrolyte are shown at the bottom of Figure 4A.
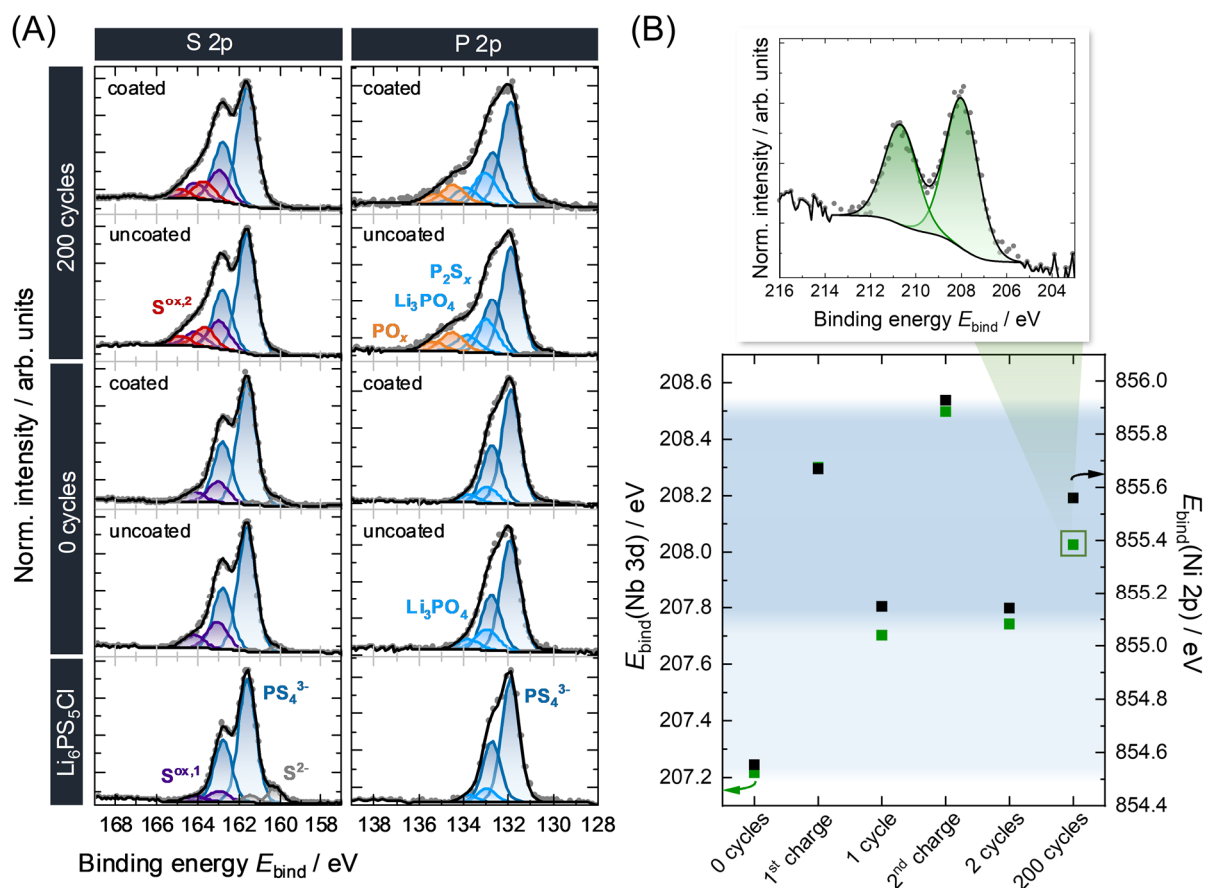
Figure 4. (A) S 2p and P 2p XP detail spectra of composite cathodes with and without $Li_2CO_3/LiNbO_3$ coating after 0 cycles and 200 cycles. Li_6PS_5Cl reference spectra are shown at the bottom. The surface was initially cleaned by sputtering with Ar^+ ions. All detail spectra were measured with a pass energy of 23.50 eV. A Shirley background and GL(30) line shapes were used for signal fitting. The XP spectra were normalized in relation to the respective signal maximum for better comparison of the signal contributions. (B) Bottom: The mean energetic signal position of the Nb 3d (green) and Ni 2p signals (black) after surface cleaning is shown at different stages of cycling. The Nb 3d signals were measured using a pass energy of 23.50 eV, whereas the pass energy for the Ni 2p ranged from 29.35 eV to 46.95 eV. The graph reveals distinct signal shifts during the first charging step for both signals (light blue area), followed by a partially reversible shift in the subsequent cycles (dark blue area). Top: The Nb 3d signal after 200 cycles is shown as an example. It can be seen that a single doublet is already sufficient to represent the experimental data. Consequently, the Nb 3d signal shape has not changed significantly during battery cycling.

15

The S 2p and P 2p contributions of the Li_6PS_5Cl reference can mainly be related to the argyrodite structure. In the S 2p signal, three contributions can be distinguished. The main component at 161.6 eV corresponds to the PS_4^{3-} units, whereas the doublet at 160.2 eV can be attributed to the free S^{2-} species of the argyrodite structure.[33,46,47] In the latter binding energy range, also Li_2S residues from the material synthesis process are conceivable.[46] For higher binding energies, a signal shoulder is visible, which can be represented in the fitting model by using a single doublet at 163.0 eV. The origin of signals in this binding energy range has often been reported and discussed for thiophosphates in literature and is mostly related to polysulfides or various anionic frameworks that Li-P-S phases can pass through during redox reactions such as $P_2S_7^{4-}$ and $P_2S_6^{2-}$ towards the formation of P_2S_5.[24,33,46–53] Because the differences in the binding energy of such compounds are very small, an unambiguous assignment without additional proof is not possible. Therefore, we labeled the doublet with the general term $S^{ox,1}$. In the P 2p signal, fitting with two doublets is already sufficient to represent the experimental data. The main component at 131.9 eV can be assigned to the PS_4^{3-} units of the argyrodite structure.[33,46,47] A further doublet can be seen at 133.0 eV. This signal is often correlated with the same compounds already mentioned for the $S^{ox,1}$ signal. In addition, Li_3PO_4 can be detected in this binding energy range, which is particularly relevant for the composite cathodes.[54,55] Accordingly, both uncycled composite cathodes (with and without CAM coating) show a slight increase in this signal contribution. Since the signal contribution is slightly decreased for the composite cathode with CAM coating, the coating seems to somewhat suppress the formation of such species. As shown in our previous experimental study, the mere NCM622/SE contact can already lead to the formation of phosphates, most probably Li_3PO_4.[24,33] This is in agreement with calculations by Xiao et al., who have shown that the contact between NCM(fully-lithiated)/Li_6PS_5Cl can trigger the formation of Li_3PO_4.[44] Interestingly, according to their work, also the LiNbO$_3$/Li_6PS_5Cl contact can lead to the formation of Li_3PO_4. Taking our experimental data into account, we assume that the driving force for the Li_3PO_4 formation is lower for the LiNbO$_3$/Li_6PS_5Cl interface. However, it must be considered that other compounds such as polysulfides (e.g. P_2S_x) can also be found in this binding energy range, which makes it difficult to clearly assign this signal with XPS alone.[46,47]

For the S 2p signals of the uncycled composite cathodes, similar effects were observed. Accordingly, $S^{ox,1}$ is increased for both composite cathodes compared to the solid electrolyte reference, while the doublet is slightly lower when using the CAM coating. Therefore, also here, our data indicate that the coating suppresses the solid electrolyte decomposition reactions caused by the mere contact of the individual materials.

In contrast, the S 2p and P 2p detail spectra of the cycled composite cathodes largely match. In both cases, battery cycling leads to an increase in the S 2p signal shoulder at higher binding energies. A single doublet at 163.7 eV is already sufficient to represent the experimental data (termed $S^{ox,2}$ in the following). The origin of signals in this binding energy range has often been discussed, analogous to $S^{ox,1}$. Based on reports on the redox-behavior of thiophosphates and recent studies on decomposition processes

in NCM and thiophosphate-based composite cathodes, we hypothesize that polysulfide formation occurs during battery cycling, which is probably accompanied by dynamic anionic framework transitions that Li-P-S phases may undergo.[24,47–50,52] Because the S 2p decomposition signals $S^{ox,1}$ and $S^{ox,2}$ are comparable in both cases, the coating seems not to significantly suppress these reactions, as can be seen from the XPS data.

In addition, both P 2p spectra show similar signal broadening. In particular, the increase of the signal shoulder at higher binding energies match to a great extent. The binding energy range of the signal shoulder indicates the formation of phosphates such as Li_3PO_4, $Ni_3(PO_4)_2$, $Mn_3(PO_4)_2$ and/or metaphosphates of these species.[36,54–56] At the same time, signal interferences with polysulfide species such as P_2S_x can be expected.[47] Overall, the P 2p spectra suggest the formation of oxygenated phosphorous species such as phosphates and metaphosphates (Li_3PO_4 and transition metal phosphates seem reasonable) and can also support the conclusions drawn from the S 2p spectra regarding the formation of polysulfides such as P_2S_x and different anionic frameworks. Analogous to the S 2p spectra, also here, the XPS results indicate that the coating does not lead to a significant decrease in decomposition product concentrations. However, it must be noted that the detection limit of XPS is comparably high. Considering the microstructure of the composite cathodes and the underlying dimensions, it becomes obvious that the small quantities of decomposition products can lead to detection limit problems. Furthermore, the deconvolution of the individual decomposition processes (current collector/solid electrolyte, carbon additive/solid electrolyte, CAM/solid electrolyte) is highly challenging due to signal interferences of decomposition products, e.g. Li_3PO_4 and P_2S_x. For this reason, we conducted ToF-SIMS measurements to reveal concentration changes below the XPS detection limit (see next section).

Interestingly, analysis of the Nb 3d signal before and after battery cycling revealed a shift in the energetic signal position. In order to investigate this effect in more detail, we analyzed the Nb 3d spectrum at different cycling stages (green data points in Figure 4B). It can be seen that the Nb 3d signal shifts strongly toward higher binding energies during the initial charging step and shifts more or less reversibly to lower and higher binding energies in subsequent cycles. Because the Ni 2p signal (black data points in Figure 4B) shows a similar trend and all spectra were calibrated in relation to solid electrolyte signals, we assume that the signal shift represents the state of charge of the CAM and is not mainly caused by a change in the chemical environment or a reaction of the coating material (a detailed discussion is given in the Supporting Information). This is supported by the fact that the potential range of the ASSB is much higher than reported values for the redox activity of $LiNbO_3$ and material-related oxides such as $LiNbO_2$ and Nb_2O_5, and the Nb 3d signal shape does not change upon cycling (see Nb 3d signal in Figure 4B).[43,57–62] It has already been shown in the literature that these effects can be exploited in XPS experiments on model systems to obtain information on electronic and ionic contributions to the electrode potential and to determine energy band diagrams experimentally.[63–66] However, since signal shifts in XP

spectra can be caused by manifold (convoluted) effects, we cannot completely exclude (electro)chemical reactions of the coating material, even though there is no direct evidence for them.

II)   Time-of-Flight Secondary Ion Mass Spectrometry.

ToF-SIMS analyses were performed to further characterize the decomposition processes in the composite cathodes below the detection limit of XPS (semi-quantitative analysis). As described in previous studies, ToF-SIMS can reveal chemical processes that are not detected by XPS due to its higher sensitivity, e.g. formation of small quantities of sulfates/sulfites as demonstrated in the following.[24,33] This makes the method particularly attractive for studies on interfacial decomposition processes in ASSBs.

Surface analyses were performed to identify decomposition products and to reveal the influence of the CAM coating. In addition, ToF-SIMS analyses on FIB crater sidewalls were performed to verify the results of the surface analysis for the bulk material and to reveal the local fragment distribution, in order to ensure that the observations can be correlated to the decomposition reactions at the CAM/solid electrolyte interface.

We analyzed composite cathodes with Li_2CO_3/$LiNbO_3$ coated NCM622 at different cycling stages (0 cycles, 1 cycle and 200 cycles) and compared the results with data obtained for composite cathode without CAM coating (0 cycles and 200 cycles).

For surface analysis, the overlap of the three different decomposition processes (current collector/solid electrolyte, carbon additive/solid electrolyte, CAM/solid electrolyte) must be taken into account, as we have described in more detail in a previous study.[24] However, despite the detrimental influence of the current collector/solid electrolyte interface, it is still possible to obtain reasonable data from ToF-SIMS surface analysis due to the higher sensitivity compared to XPS. Based on experience, XPS investigations inevitably require surface cleaning, since results of surface measurements differ significantly from depth profiling results. This makes it often almost impossible to obtain reliable data. In contrast, ToF-SIMS surface spectra often show comparable results to depth profiling as shown earlier.[24,33] However, to minimize the effect of analysis area dependence it is necessary to increase the statistics. Therefore, ten measurements per sample were performed (the scattering of the data is indicated by the boxplots in Figure 5A).

According to previous work with ToF-SIMS, phosphate (PO_x^-) and sulfate/sulfite (SO_x^-) fragments are of particular interest in the context of the decomposition of thiophosphate-based composite cathodes.[24,33,67] Figure 5A illustrate the results of the surface analysis related to phosphate and sulfate/sulfite fragments in boxplots.

From the surface analysis, it is evident that battery cycling leads in both cases (uncoated and coated CAM) to significant increases in phosphate and sulfate/sulfite fragments. The results for the composite

cathodes containing the Li_2CO_3/$LiNbO_3$ coated CAM indicate that the formation of decomposition products occurs successively and is not completed after the first cycle. This is in accordance with our XPS results (see Supporting Information Figure S6). After 200 cycles, the composite cathode with coated CAM shows decreased intensities for PO_x^- and SO_x^- fragments compared to the uncoated reference. This indicates that the Li_2CO_3/$LiNbO_3$ coating suppresses the formation of phosphates and sulfates/sulfites.
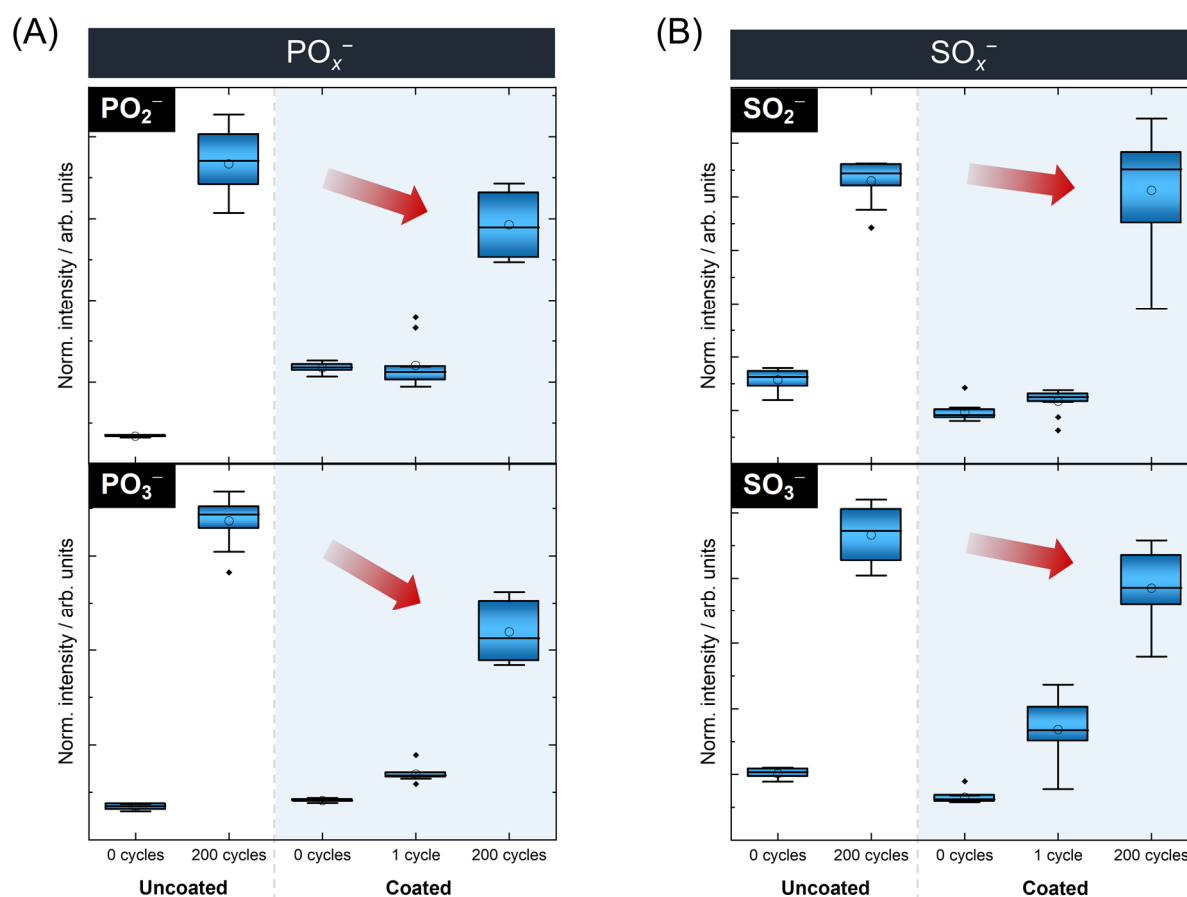
Figure 5. Results from ToF-SIMS surface analyses. Shown are boxplots of the normalized intensity of PO_x^- and SO_x^- fragments (with $2 \leq x \leq 3$). The primary ion gun was operated in spectrometry mode (bunched mode) using Bi_3^+(25 keV) as primary ion species. Ten mass spectra were measured for each sample to minimize effects of the analysis area dependence. Electrochemical cycling leads in both cases (coated and uncoated) to significant increases in PO_x^- and SO_x^- fragments. The Li_2CO_3/$LiNbO_3$ coating is capable of somewhat suppressing the formation of phosphates and sulfates/sulfites.

For the uncycled composite cathodes, the sulfates/sulfites formation due to the mere NCM/solid electrolyte contact seems suppressed. This indicates, analogous to the XPS results, a suppression of the interfacial reaction due to the mere NCM/SE contact. This is also in accordance with calculations by Xiao *et al*., who have shown that Li_2SO_4 is a favorable reaction product for NCM/Li_6PS_5Cl interfaces, whereas this is not the case for the $LiNbO_3$/Li_6PS_5Cl interface.[44]

In contrast, the suppression of the interfacial reaction is not as obvious for the phosphate fragments, which at first glance seems to contradict the XPS results. However, it should be noted that PO_2^- and PO_3^- show different trends (compare 0 cycles with 1 cycle for the coated case), which could be due to mass interferences. In addition, we cannot neglect the decomposition process overlap with the current collector/solid electrolyte interface in surface analyses. Indeed, we will show later that ToF-SIMS analyses on FIB crater sidewalls confirm the XPS results. Since the current collector/solid electrolyte interface influence can be excluded in these measurements, we assume a detrimental influence by the current collector here.[24]

In the next step, we analyzed FIB crater sidewalls to verify the surface analysis results for the bulk material and to reveal the local fragment distribution with high lateral resolution. The latter is particularly important, in order to confirm that the results obtained can be correlated to the decomposition reactions at the CAM/solid electrolyte interface. It should be noted here that the maximum lateral resolution theoretically achieved is 122 nm (see Experimental Section). However, due to the topographic effects and the inclined nature of the crater, this value should be interpreted as the maximum resolution under ideal conditions.

Figure 6A shows exemplary secondary ion images of the crater sidewall for the composite cathode with coated CAM after 200 cycles. The different components of the composite can be easily distinguished from each other using specific fragments. Accordingly, the NCM622 particles (NiO_2^- fragment), the Li_6PS_5Cl solid electrolyte (Cl^-), the CAM coating (NbO_3^-) and the decomposition layer (PO_x^- and SO_x^-) can be represented very well with high lateral resolution. The local distribution of phosphate and sulfate/sulfite fragments was studied by multiplication of secondary ion images to eliminate mass interferences analogously to our previous work.[33]

For the uncycled composite cathodes, the secondary ion images revealed that phosphate and sulfate/sulfite formation already takes place due to the mere material contact at the CAM/solid electrolyte interface. Battery cycling leads to a further increase in phosphate and sulfate/sulfite signals regardless of the CAM coating.[24,33]

For the composite cathode with coated CAM, even after 200 cycles, the coating fragment NbO_3^- can still be detected around the NCM622 secondary particles (Figure 6A). Therefore, a significant consumption/dissolution of the coating due to diffusion and (electro)chemical reactions does not seem to take place. Nevertheless, from the secondary ion images, it is apparent that phosphate (PO_x^-) and sulfate/sulfite (SO_x^-) formation still occurs at the NCM/solid electrolyte interface, despite CAM coating.

In this context, the question arises whether there are differences in the detected decomposition product concentrations. To draw semi-quantitative conclusions, a ROI analysis was performed analogous to previous studies.[24,33,68] The procedure of such an analysis is described in more detail in the Supporting Information. The results of the ROI analysis are shown in Figure 6B.

For the uncycled composite cathodes, comparable trends to the XPS analysis can be observed. Accordingly, the composite cathode containing the coated CAM shows a suppressed interfacial reaction due to the mere CAM/solid electrolyte contact, indicated by the lower amount of phosphate and sulfate/sulfite fragments. From the data for the composite cathodes containing coated CAM, it can be seen that the formation of such species is not completed after the first cycle but rather gradually increases during battery cycling, which is in accordance with our XPS results (see Supporting Information Figure S6).

After 200 cycles, the intensity of PO_x^- and SO_x^- fragments is significantly increased in both cases, but the protective nature of the CAM coating is clearly evident, as the signal intensities are lower in this case.
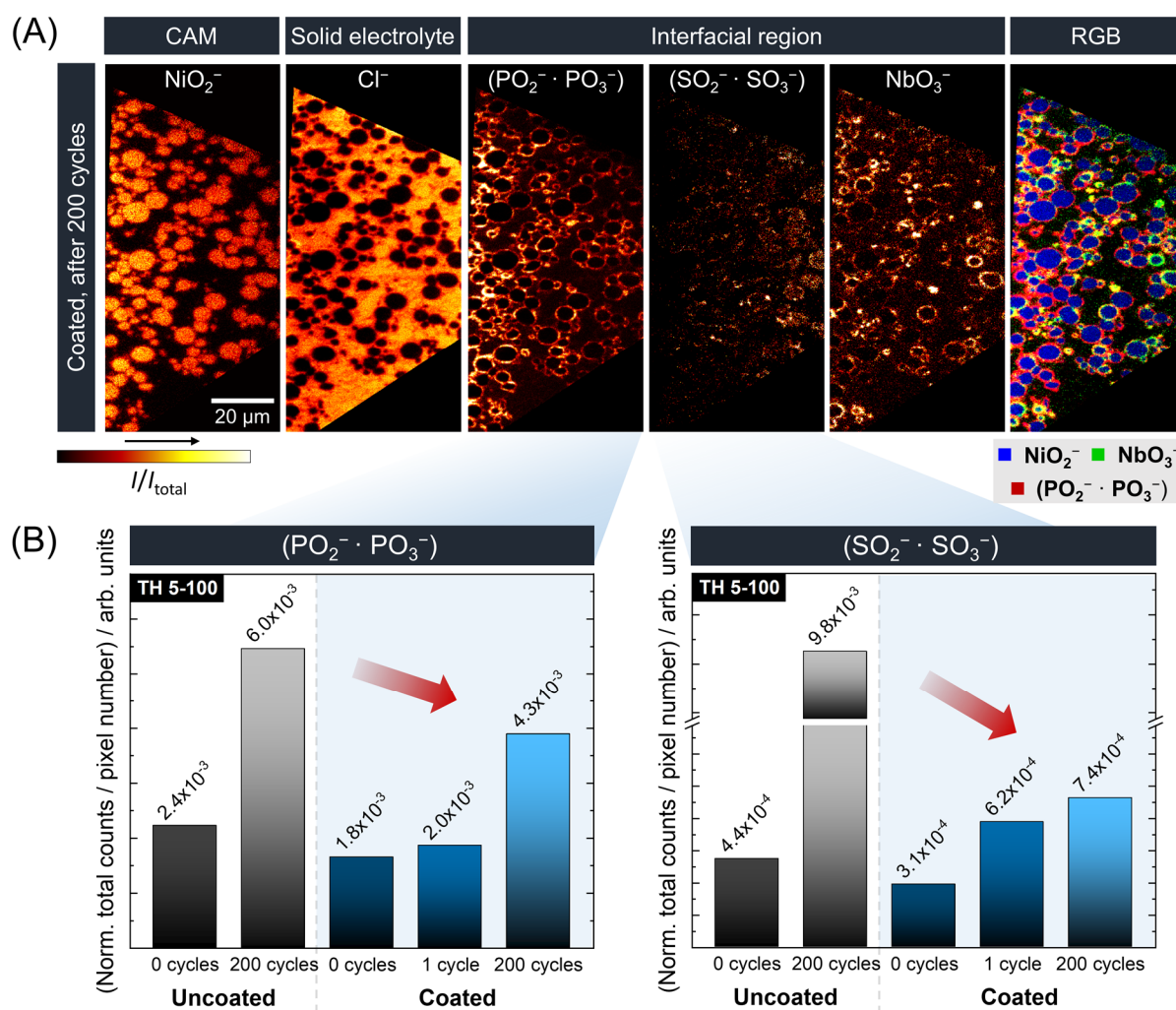
Figure 6. (A) ToF-SIMS measurement on a 45° crater sidewall of the cycled composite cathode with $Li_2CO_3/LiNbO_3$ coated NCM622. Shown are exemplary secondary ion images of negatively charged fragments and a RGB overlay. The cathode active material (NiO_2^-), the coating (NbO_3^-), the solid electrolyte (Cl^-) and the degradation layer (($PO_2^- \cdot PO_3^-$) and ($SO_2^- \cdot SO_3^-$)) can be clearly distinguished from each other. (B) Results of the ROI analysis for the multiplied ($PO_2^- \cdot PO_3^-$) and ($SO_2^- \cdot SO_3^-$) secondary ion images. Battery cycling leads to an increase in phosphate and sulfate/sulfite fragments. The $Li_2CO_3/LiNbO_3$ coating suppresses the reaction at the CAM/solid electrolyte interface.

21

Overall, the SIMS results indicate a suppression of the interfacial reaction at the CAM/solid electrolyte interface and highlight the suitability of the method for such investigations. The XPS results related to the interfacial reaction by mere contact could be confirmed. In addition, the high sensitivity of the method allowed the detection of concentration differences for phosphates and sulfates/sulfites in the CAM/solid electrolyte interface region that could not be resolved with XPS.

Discussion

In the following, we summarize the main findings of the results section and discuss them in the context of published work. First, we address the coating microstructure, especially its morphology and chemical composition. Based on this knowledge, we then discuss the influence of the CAM coating on the battery performance and the decomposition processes in the composite cathodes.

1. Coating Microstructure.

The coating approach in this work led to a particulate coating with a mean layer thickness of ~15 nm. According to our XPS and ToF-SIMS data, the coating particles consists of a $LiNbO_3$ core, a Li_2CO_3 shell and small quantities of carbon-containing residues from the coating procedure. It can be assumed that the $LiNbO_3$ core is in an amorphous state, since the heating temperature was only 300 °C and the crystallization temperature is usually ≥460 °C.[42,43] It has already been demonstrated that the amorphous phase exhibits a much higher lithium ion conductivity compared to single-crystalline $LiNbO_3$, whereas the transport properties are reported to be strongly dependent on the grain boundary microstructure.[42,69] It should be noted that small deviations from the here postulated stoichiometry are virtually impossible to detect. The microstructure and spherical geometry of CAMs are not ideal for most analytical methods, and the small dimensions and concentration of the coating material are often in the range of the detection limit. Even the common combination of TEM, EDX and EELS is, according to Kim et al., limited to basic statements about the local layer thickness and element distribution for a $Li_2CO_3/LiNbO_3$ hybrid coating and does not provide further insights into the coating microstructure.[26]

Calculations by Xiao et al. suggest that NCM (fully-lithiated) can react with $LiNbO_3$ to form compounds such as Li_3NbO_4, $LiMnCoO_4$ and NiO.[44] However, the reaction energy and thus the driving force for the reaction of $LiNbO_3$ with fully-lithiated NCM is comparably small. This is further supported by calculations of Nolan et al.[45] In addition, the half-lithiated Ni-rich cathode/$LiNbO_3$ interface should be stable.[44,45] Therefore, we do not assume a strong effect and expect only very low product concentrations in the interfacial region. Indeed, experimental identification of such compounds was not possible in this work. In addition to detection limitations of the analytical instruments, considering the chemical similarity of possible products, small binding energy differences in XP spectra and similar fragmentations in ToF-SIMS spectra further complicate analyses in this direction. For this reason, we cannot provide further insight into the reaction of the coating and CAM here.

2. Influence of the Coating on the ASSB Performance and the CAM/Solid Electrolyte Interfacial Decomposition.

In general, the Li_2CO_3/$LiNbO_3$ coating leads to a significant improvement in long-term cycling performance. Accordingly, the absolute capacities are enhanced and the capacity fading during cycling is reduced. However, considering that a less-pronounced but steady capacity fading is still visible, detrimental interfacial reactions are still occurring in the composite cathode. In this context, it must be taken into account, that interfacial reactions can generally occur at three different interfaces in composite cathodes: i) current collector/solid electrolyte, ii) carbon additive/solid electrolyte, iii) CAM/solid electrolyte.[24] Since we only applied a protective coating to the CAM, we still expect unaffected detrimental interfacial reactions at the interfaces i) and ii).

The detrimental effect of carbon additives on the ASSB performance has already been investigated in the past.[24,32,70,71] Reports on the interfacial reaction of carbon with thiophosphates indicate decomposition products such as polysulfides and/or various anionic frameworks that Li-P-S phases can pass through during redox reactions.[24,50] Because the decomposition products from the interfaces ii) and iii) overlap in the S 2p spectra, it is almost impossible to separate the individual contributions. Hence, the pronounced formation of the signal shoulder at higher binding energies in the S 2p signal during battery cycling (Figure 4A) can partially be explained by reactions at the carbon additive/solid electrolyte interface. A further hint in this direction is, that the formation of this signal shoulder is already almost completed after the initial cycles (Figure S6). In contrast, species that can be more clearly associated with interface reactions at the CAM/solid electrolyte interface such as phosphates and sulfates/sulfites (which require an oxygen source) tend to form successively. This is indicated by the P 2p signal (Figure S6) as well as by ToF-SIMS investigations (Figure 5 and Figure 6). Strategies to overcome the interfacial reaction at the carbon additive/solid electrolyte interface have already been demonstrated and have been shown to improve the performance of ASSBs.[72,73] Analogous to the CAM, this often comprises coating approaches.

Despite the decomposition overlap, our post-mortem analysis clearly revealed reactions that can unambiguously be attributed to the CAM/solid electrolyte interface. For the uncoated CAM, the XPS and ToF-SIMS data indicate distinct formation of oxygenated phosphorous and sulfur species such as phosphates and sulfates/sulfites. This is consistent with previous experimental and computational studies in the context of thiophosphate-based composite cathodes.[24,33,44,67,74,75] We have already proposed a scheme for the NCM622/β-Li_3PS_4 interfacial reaction in a previous study.[24] Since we find comparable results for the NCM622/Li_6PS_5Cl, similar reactions are likely to occur. Considering recent calculations, we assume that thermodynamically preferred reaction paths involve the formation of transition metal sulfides as intermediate products, which ultimately react to phosphates and sulfates in a metathesis-type reaction.[24,44,74,75] In this context, it should be noted that, in contrast to other experimental work, there is

no clear evidence of transition metal sulfide formation in our XPS and ToF-SIMS data.[27,76,77] In a previous work, we have already discussed the possibility of a misleading energy calibration of XP spectra and thus a misleading detection of transition metal sulfides.[24] Apart from the possibility of a metathesis-type reaction, the formation of oxygenated phosphorous and sulfur compounds can also be partially ascribed to the chemical reaction of released O_2 (partially present as highly reactive singlet $^1O_2$) during battery cycling, either from the NCM lattice at high states of charge or from the electrochemical decomposition of Li_2CO_3 as reported in literature.[26,78–83]

Overall, the interfacial reactions at the CAM/solid electrolyte interface leads to the formation of oxygenated phosphorus and sulfur species which can be accompanied by a formation of a rock-salt-like CAM phase.[24] In addition, we assume that oxidized – but not oxygenated – sulfur species such as polysulfides form near the interfaces due to electrochemical decomposition of the solid electrolyte (analogous to the current collector/solid electrolyte and carbon additive/solid electrolyte interfaces). Products such as Li_3PO_4, Li_2SO_4 and polysulfides tend to reduce the partial ionic conductivity locally in the interface region compared to the pristine CAM and solid electrolyte, resulting in an increase in resistance and thus a decrease in ASSB performance.[48,84–88] However, the actual properties of the interface layer formed depend largely on the compounds present, their precise stoichiometry and their microstructure. Even for a single material in the interface region such as $LiNbO_3$, the materials´ properties can vary significantly due to the crystallinity, defects and the microstructure of the material (e.g., bulk vs. grain boundary properties).[42,69] The complexity is further increased when interactions with other compounds in the interface region are considered. In model-type experiments, pseudo-binary and pseudo-ternary phases and phase mixtures containing Li_3PO_4, Li_2SO_4 and Li_2CO_3, which are all reasonable compounds of interface layers, the influence of composition on electronic and ionic partial conductivities has already been systematically studied and was found to be strong.[85,89–91] Considering the low product fractions and the small dimension of the degradation layer (nm range), the unequivocal experimental identification of specific compounds and their stoichiometries remains an enormous analytical challenge.

The Li_2CO_3/$LiNbO_3$ coating reduces, but does not completely suppresses the aforementioned interfacial reactions at the CAM/solid electrolyte interface, which is particular evident from the ToF-SIMS results (Figure 5 and Figure 6). These findings are in accordance to a study by Visbal et al., who observed similar trends by near-surface ToF-SIMS analyses for a diamond-like carbon coating on $LiNi_{0.8}Co_{0.15}Al_{0.05}O_2$ (NCA) in an amorphous Li_2S-P_2S_5 (75:25 mol%)-based composite cathode.[67] This suggests that the effects described seem somehow universal for thiophosphate-based ASSBs.

However, since the interfacial reaction cannot be completely prevented by the Li_2CO_3/$LiNbO_3$ coating, the question for the reason of this imperfect function arises. The remaining interfacial degradation can be related to the microstructure of the coating, namely the coating morphology and coating composition.

The coating morphology is particulate. This implies the presence of uncoated/less-coated areas, where the interfacial reaction can occur almost unhindered. A homogenous layer is therefore preferable as a

protective coating but often difficult to achieve experimentally. In addition, partial mechanical abrasion of the coating during cell assembly is conceivable, and chemo-mechanical volume changes during cell cycling can lead to exposure of uncoated areas.[92] Besides the morphology, also the coating composition seems not ideal under consideration of the calculated stability against thiophosphate-based solid electrolytes.[44,93] According to Xiao *et al.*, the material combination $LiNbO_3/Li_6PS_5Cl$ has a non-negligible negative reaction energy, which can lead to the formation of Li_3PO_4 among other products.[44] Consequently, phosphate fragments can partially also be related to the $LiNbO_3/Li_6PS_5Cl$ interface. However, the reaction energy is smaller compared to the bare NCM/Li_6PS_5Cl material combination, thus leading to a reduced driving force for the interfacial reaction. This is in accordance with our analytical results before and after battery cycling, showing a suppressed formation of decomposition products with the $Li_2CO_3/LiNbO_3$ coating.

The role of the Li_2CO_3 content in the coating is yet not completely clear. Kim et al. demonstrated that Li_2CO_3 alone may already have a beneficial effect on the ASSB performance compared to uncoated CAM.[26] However, according to a recent study by Strauss et al., the Li_2CO_3 content in the coating must be specifically tailored to the coating used.[83] The positive effect of Li_2CO_3 in many coatings can have various reasons: Taking the typical solid-state synthesis of lithium transition metal oxides such as $LiNbO_3$ from Li_2CO_3 and Nb_2O_5 into account, a stabilizing effect of Li_2CO_3 on $LiNbO_3$ could be conceivable.[94] Considering the particulate nature of the coating, it is also possible that the positive influence of Li_2CO_3 is due to the fact that Li_2CO_3 prevents direct contact of the CAM with the solid electrolyte in less coated/uncoated areas between the coating particles. Accordingly, the Li_2CO_3 would compensate for the deficiencies of the coating microstructure and the optimum content of Li_2CO_3 would depend on the coating material and its overall microstructure. Therefore, we do not assume the Li_2CO_3 to be generally detrimental here. Nevertheless, as indicated by calculations, $LiNbO_3$ and probably also Li_2CO_3 do not seem to be the best choice and other coating materials should be more beneficial to suppress the interface reaction at the CAM/solid electrolyte interface.[44,45,93] In addition to the interface stability of the materials, it must be noted that materials´ properties such as ionic and electrical partial conductivity play an important role in the choice of coating materials.[95] Since Li_2CO_3 has a relatively low ionic conductivity, it is certainly not an ideal coating material, although it seems to be able to partially stabilize the CAM/solid electrolyte interface compared to the uncoated interface.[96] Consequently, further optimization of the coating composition and the coating microstructure remains an important step towards long-term stable ASSBs.

Overall, the working principle of the $Li_2CO_3/LiNbO_3$ coating in this work can be related to the suppression of the interfacial reaction at the CAM/solid electrolyte interface. This leads to a reduced formation of phosphates (likely Li_3PO_4 and transition metal phosphates) and sulfates/sulfites (likely Li_2SO_4 and transition metal sulfates). Because the ionization probability of negatively charged phosphate and sulfate/sulfite fragments is basically high, ToF-SIMS is an excellent analytical method to investigate the

protective effect of coating in thiophosphate-based composite cathodes. In principle, it should be possible in this way to semi-quantitatively benchmark the efficiency of protective coatings in suppressing interfacial reactions by using ToF-SIMS.

Conclusions

We investigated the influence of a $Li_2CO_3/LiNbO_3$ coating on $LiNi_{0.6}Co_{0.2}Mn_{0.2}O_2$ on the battery performance and the decomposition processes on the positive electrode side of a $Li_4Ti_5O_{12}$/Super C65 | Li_6PS_5Cl | NCM622/Li_6PS_5Cl/Super C65 ASSB cell.

The coating microstructure is characterized in terms of morphology and chemical composition. A combination of FIB-SEM, XPS and ToF-SIMS reveals a particulate coating with a mean layer thickness of ~15 nm. The coating particles consist of an amorphous $LiNbO_3$ core, a Li_2CO_3 shell and small quantities of carbon-containing residues form the coating procedure.

Electrochemical investigations reveal the positive effect of the protective coating on the ASSB performance. Accordingly, the capacity fading during cycling is decreased and thus the long-term cycling performance is significantly enhanced. Because the particulate character of the coating allows for unprotected areas and the coating composition is not ideal in terms of stability against the solid electrolyte, a less pronounced but steady capacity fading still occurs.

Comprehensive post-mortem analyses of composite cathodes by using a combination of XPS and ToF-SIMS show that the CAM coating successfully suppresses the interfacial reaction at the CAM/solid electrolyte interface in terms of reduced formation of oxygenated phosphorous and sulfur compounds such as phosphates and sulfates/sulfites. In addition, we show that the formation of decomposition products in the interfacial region is successive and not fully completed after the initial cycles.

Overall, this work extends the knowledge of the working principle of protective coatings. This will help to better understand the protective nature of coatings and to design tailored CAM coatings and interfaces in the future. We also highlighted the suitability of ToF-SIMS for investigations on decomposition processes occurring in thiophosphate-based ASSBs. In principle, this allows for semi-quantitatively benchmarking the influence of protective coatings on the decomposition processes in thiophosphate-based composite cathodes.

Associated Content

Supporting Information

SEM images of the coated NCM622 secondary particles, ATR-IR spectra of the uncoated and the Li_2CO_3/$LiNbO_3$ coated NCM622, Coulomb efficiency as a function of the cycle number, XP spectra of the Cl 2p, O 1s, Li 1s and C 1s signals of a Li_6PS_5Cl reference and the (un)cycled composite cathodes, discussion on the Nb 3d shift in XP spectra, S 2p and P 2p detail spectra of composite cathodes with Li_2CO_3/$LiNbO_3$ coated NCM622 at different cycling stages, ROI analysis procedure scheme, results of ROI analysis for different signal thresholds.

Author Information

Corresponding Authors

*E-mail: Juergen.Janek@phys.Chemie.uni-giessen.de

ORCID

Florian Strauss: 0000-0001-5817-6349

Joachim Sann: 0000-0003-4663-2671

Marcus Rohnke: 0000-0002-8867-950X

Torsten Brezesinski: 0000-0002-4336-263X

Jürgen Janek: 0000-0002-9221-4756

Notes

The authors declare no competing financial interest.

Acknowledgments

References

(1)   Seino, Y.; Ota, T.; Takada, K.; Hayashi, A.; Tatsumisago, M. A Sulphide Lithium Super Ion Conductor Is Superior to Liquid Ion Conductors for Use in Rechargeable Batteries. *Energy Environ. Sci.* **2014**, *7* (2), 627–631. https://doi.org/10.1039/c3ee41655k.

(2)   Janek, J.; Zeier, W. G. A Solid Future for Battery Development. *Nat. Energy* **2016**, *1* (9), 16141. https://doi.org/10.1038/nenergy.2016.141.

(3)   Xu, W.; Wang, J.; Ding, F.; Chen, X.; Nasybulin, E.; Zhang, Y.; Zhang, J.-G. Lithium Metal Anodes for Rechargeable Batteries. *Energy Environ. Sci.* **2014**, *7* (2), 513–537. https://doi.org/10.1039/c3ee40795k.

(4)   Ulvestad, A. A Brief Review of Current Lithium Ion Battery Technology and Potential Solid State Battery Technologies. 2018, arXiv:1803.04317. arXiv.org e-Print archive. https://arxiv.org/abs/ 1803.04317 (accessed November 5, 2020).

(5)   Lee, Y.; Fujiki, S.; Jung, C.; Suzuki, N.; Yashiro, N.; Omoda, R.; Ko, D.; Shiratsuchi, T.; Sugimoto, T.; Ryu, S.; et al. High-Energy Long-Cycling All-Solid-State Lithium Metal Batteries Enabled by Silver–Carbon Composite Anodes. *Nat. Energy* **2020**, *5* (4), 299–308. https://doi.org/10.1038/s41560-020-0575-z.

(6)   Randau, S.; Weber, D. A.; Kötz, O.; Koerver, R.; Braun, P.; Weber, A.; Ivers-Tiffée, E.; Adermann, T.; Kulisch, J.; Zeier, W. G.; et al. Benchmarking the Performance of All-Solid-State Lithium Batteries. *Nat. Energy* **2020**, *5* (3), 259–270. https://doi.org/10.1038/s41560-020-0565-1.

(7)   Schnell, J.; Günther, T.; Knoche, T.; Vieider, C.; Köhler, L.; Just, A.; Keller, M.; Passerini, S.; Reinhart, G. All-Solid-State Lithium-Ion and Lithium Metal Batteries – Paving the Way to Large-Scale Production. *J. Power Sources* **2018**, *382*, 160–175. https://doi.org/10.1016/j.jpowsour.2018.02.062.

(8)   Goodenough, J. B.; Kim, Y. Challenges for Rechargeable Li Batteries. *Chem. Mater.* **2010**, *22* (3), 587–603. https://doi.org/10.1021/cm901452z.

(9)   Ding, Y.; Cano, Z. P.; Yu, A.; Lu, J.; Chen, Z. Automotive Li-Ion Batteries: Current Status and Future Perspectives. *Electrochem. Energy Rev.* **2019**, *2* (1), 1–28. https://doi.org/10.1007/s41918-018-0022-z.

(10)   Chen, R.; Li, Q.; Yu, X.; Chen, L.; Li, H. Approaching Practically Accessible Solid-State Batteries: Stability Issues Related to Solid Electrolytes and Interfaces. *Chem. Rev.* **2020**, *120* (14), 6820–6877. https://doi.org/10.1021/acs.chemrev.9b00268.

(11)   Lee, H.; Oh, P.; Kim, J.; Cha, H.; Chae, S.; Lee, S.; Cho, J. Advances and Prospects of Sulfide All-Solid-State Lithium Batteries via One-to-One Comparison with Conventional Liquid Lithium Ion Batteries. *Adv. Mater.* **2019**, *31* (29), 1–26. https://doi.org/10.1002/adma.201900376.

(12)   Famprikis, T.; Canepa, P.; Dawson, J. A.; Islam, M. S.; Masquelier, C. Fundamentals of Inorganic Solid-State Electrolytes for Batteries. *Nat. Mater.* **2019**, *18* (12), 1278–1291. https://doi.org/10.1038/s41563-019-0431-3.

(13)   Wang, S.; Fang, R.; Li, Y.; Liu, Y.; Xin, C.; Richter, F. H.; Nan, C.-W. Interfacial Challenges for All-Solid-State Batteries Based on Sulfide Solid Electrolytes. *J. Mater.* **2021**, *7* (2), 209–218. https://doi.org/10.1016/j.jmat.2020.09.003.

(14)   Bielefeld, A.; Weber, D. A.; Janek, J. Microstructural Modeling of Composite Cathodes for All-Solid-State Batteries. *J. Phys. Chem. C* **2019**, *123* (3), 1626–1634. https://doi.org/10.1021/acs.jpcc.8b11043.

(15)   Shi, T.; Tu, Q.; Tian, Y.; Xiao, Y.; Miara, L. J.; Kononova, O.; Ceder, G. High Active Material Loading in All-Solid-State Battery Electrode via Particle Size Optimization. *Adv. Energy Mater.* **2019**, *10* (1), 1902881. https://doi.org/10.1002/aenm.201902881.

(16)   Bielefeld, A.; Weber, D. A.; Janek, J. Modeling Effective Ionic Conductivity and Binder Influence in Composite Cathodes for All-Solid-State Batteries. *ACS Appl. Mater. Interfaces* **2020**, *12* (11), 12821–12833. https://doi.org/10.1021/acsami.9b22788.

(17)   Neumann, A.; Randau, S.; Becker-Steinberger, K.; Danner, T.; Hein, S.; Ning, Z.; Marrow, J.; Richter, F. H.; Janek, J.; Latz, A. Analysis of Interfacial Effects in All-Solid-State Batteries with Thiophosphate Solid Electrolytes. *ACS Appl. Mater. Interfaces* **2020**, *12* (8), 9277–9291. https://doi.org/10.1021/acsami.9b21404.

(18)   Park, J.; Kim, K. T.; Oh, D. Y.; Jin, D.; Kim, D.; Jung, Y. S.; Lee, Y. M. Digital Twin-Driven All-Solid-State Battery: Unraveling the Physical and Electrochemical Behaviors. *Adv. Energy Mater.* **2020**, *2001563*, 2001563. https://doi.org/10.1002/aenm.202001563.

(19)   Park, K.-H.; Kaup, K.; Assoud, A.; Zhang, Q.; Wu, X.; Nazar, L. F. High-Voltage Superionic Halide Solid Electrolytes for All-Solid-State Li-Ion Batteries. *ACS Energy Lett.* **2020**, *5* (2), 533–539. https://doi.org/10.1021/acsenergylett.9b02599.

(20)   Gent, W. E.; Abate, I. I.; Yang, W.; Nazar, L. F.; Chueh, W. C. Design Rules for High-Valent Redox in Intercalation Electrodes. *Joule* **2020**, *4* (7), 1369–1397. https://doi.org/10.1016/j.joule.2020.05.004.

(21)   Culver, S. P.; Koerver, R.; Zeier, W. G.; Janek, J. On the Functionality of Coatings for Cathode

Active Materials in Thiophosphate-Based All-Solid-State Batteries. *Adv. Energy Mater.* **2019**, *9* (24), 1900626. https://doi.org/10.1002/aenm.201900626.

(22) Gurung, A.; Pokharel, J.; Baniya, A.; Pathak, R.; Chen, K.; Lamsal, B. S.; Ghimire, N.; Zhang, W.-H.; Zhou, Y.; Qiao, Q. A Review on Strategies Addressing Interface Incompatibilities in Inorganic All-Solid-State Lithium Batteries. *Sustain. Energy Fuels* **2019**, *3* (12), 3279–3309. https://doi.org/10.1039/C9SE00549H.

(23) Zhang, X.-D.; Yue, F.-S.; Liang, J.-Y.; Shi, J.-L.; Li, H.; Guo, Y.-G. Structure Design of Cathode Electrodes for Solid-State Batteries: Challenges and Progress. *Small Struct.* **2020**, *1* (3), 2000042. https://doi.org/10.1002/sstr.202000042.

(24) Walther, F.; Randau, S.; Schneider, Y.; Sann, J.; Rohnke, M.; Richter, F. H.; Zeier, W. G.; Janek, J. Influence of Carbon Additives on the Decomposition Pathways in Cathodes of Lithium Thiophosphate-Based All-Solid-State Batteries. *Chem. Mater.* **2020**, *32* (14), 6123–6136. https://doi.org/10.1021/acs.chemmater.0c01825.

(25) Ohta, N.; Takada, K.; Sakaguchi, I.; Zhang, L.; Ma, R.; Fukuda, K.; Osada, M.; Sasaki, T. $LiNbO_3$-Coated $LiCoO_2$ as Cathode Material for All Solid-State Lithium Secondary Batteries. *Electrochem. commun.* **2007**, *9* (7), 1486–1490. https://doi.org/10.1016/j.elecom.2007.02.008.

(26) Kim, A.-Y.; Strauss, F.; Bartsch, T.; Teo, J. H.; Hatsukade, T.; Mazilkin, A.; Janek, J.; Hartmann, P.; Brezesinski, T. Stabilizing Effect of a Hybrid Surface Coating on a Ni-Rich NCM Cathode Material in All-Solid-State Batteries. *Chem. Mater.* **2019**, *31* (23), 9664–9672. https://doi.org/10.1021/acs.chemmater.9b02947.

(27) Jung, S.-K.; Gwon, H.; Lee, S.-S.; Kim, H.; Lee, J. C.; Chung, J. G.; Park, S. Y.; Aihara, Y.; Im, D. Understanding the Effects of Chemical Reactions at the Cathode–Electrolyte Interface in Sulfide Based All-Solid-State Batteries. *J. Mater. Chem. A* **2019**, *7* (40), 22967–22976. https://doi.org/10.1039/c9ta08517c.

(28) Jung, S. H.; Oh, K.; Nam, Y. J.; Oh, D. Y.; Brüner, P.; Kang, K.; Jung, Y. S. Li_3BO_3–Li_2CO_3: Rationally Designed Buffering Phase for Sulfide All-Solid-State Li-Ion Batteries. *Chem. Mater.* **2018**, *30* (22), 8190–8200. https://doi.org/10.1021/acs.chemmater.8b03321.

(29) Xiong, X.; Wang, Z.; Yue, P.; Guo, H.; Wu, F.; Wang, J.; Li, X. Washing Effects on Electrochemical Performance and Storage Characteristics of $LiNi_{0.8}Co_{0.1}Mn_{0.1}O_2$ as Cathode Material for Lithium-Ion Batteries. *J. Power Sources* **2013**, *222*, 318–325. https://doi.org/10.1016/j.jpowsour.2012.08.029.

(30) Nam, Y. J.; Park, K. H.; Oh, D. Y.; An, W. H.; Jung, Y. S. Diagnosis of Failure Modes for All-Solid-State Li-Ion Batteries Enabled by Three-Electrode Cells. *J. Mater. Chem. A* **2018**, *6* (30),

14867–14875. https://doi.org/10.1039/c8ta03450h.

(31)   Strauss, F.; Bartsch, T.; de Biasi, L.; Kim, A.-Y.; Janek, J.; Hartmann, P.; Brezesinski, T.
        Impact of Cathode Material Particle Size on the Capacity of Bulk-Type All-Solid-State
        Batteries. *ACS Energy Lett.* **2018**, *3* (4), 992–996.
        https://doi.org/10.1021/acsenergylett.8b00275.

(32)   Strauss, F.; Stepien, D.; Maibach, J.; Pfaffmann, L.; Indris, S.; Hartmann, P.; Brezesinski, T.
        Influence of Electronically Conductive Additives on the Cycling Performance of Argyrodite-
        Based All-Solid-State Batteries. *RSC Adv.* **2019**, *10* (2), 1114–1119.
        https://doi.org/10.1039/c9ra10253a.

(33)   Walther, F.; Koerver, R.; Fuchs, T.; Ohno, S.; Sann, J.; Rohnke, M.; Zeier, W. G.; Janek, J.
        Visualization of the Interfacial Decomposition of Composite Cathodes in Argyrodite-Based
        All-Solid-State Batteries Using Time-of-Flight Secondary-Ion Mass Spectrometry. *Chem.
        Mater.* **2019**, *31* (10), 3745–3755. https://doi.org/10.1021/acs.chemmater.9b00770.

(34)   Maibach, J.; Lindgren, F.; Eriksson, H.; Edström, K.; Hahlin, M. Electric Potential Gradient at
        the Buried Interface between Lithium-Ion Battery Electrodes and the SEI Observed Using
        Photoelectron Spectroscopy. *J. Phys. Chem. Lett.* **2016**, *7* (10), 1775–1780.
        https://doi.org/10.1021/acs.jpclett.6b00391.

(35)   Lindgren, F.; Rehnlund, D.; Källquist, I.; Nyholm, L.; Edström, K.; Hahlin, M.; Maibach, J.
        Breaking Down a Complex System: Interpreting PES Peak Positions for Cycled Li-Ion Battery
        Electrodes. *J. Phys. Chem. C* **2017**, *121* (49), 27303–27312.
        https://doi.org/10.1021/acs.jpcc.7b08923.

(36)   Moulder, J. F.; Stickle, W. F.; Sobol, P. E.; Bomben, K. D. *Handbook of X-Ray Photoelectron
        Spectroscopy; A Reference Book of Standard Spectra for Identification and Interpretation of
        XPS Data*; Chastain, J., King Jr., R. C., Eds.; Physical Electronics: Eden Prairie, US-MN, 1995.

(37)   Iwanowski, R. J.; Heinonen, M.; Pracka, I.; Raczyńska, J.; Fronc, K.; Sobczak, J. W.
        Application of in Situ Surface Scraping for Extracting Bulk Component of XPS Signal –
        Example of $LiNbO_3$ and GaSb. *J. Alloys Compd.* **1999**, *286* (1–2), 162–166.
        https://doi.org/10.1016/S0925-8388(98)01000-7.

(38)   Skryleva, E. A.; Kubasov, I. V.; Kiryukhantsev-Korneev, P. V.; Senatulin, B. R.; Zhukov, R.
        N.; Zakutailov, K. V.; Malinkovich, M. D.; Parkhomenko, Y. N. XPS Study of Li/Nb Ratio in
        $LiNbO_3$ Crystals. Effect of Polarity and Mechanical Processing on $LiNbO_3$ Surface Chemical
        Composition. *Appl. Surf. Sci.* **2016**, *389*, 387–394.
        https://doi.org/10.1016/j.apsusc.2016.07.108.

(39)   Kanamura, K.; Tamura, H.; Shiraishi, S.; Takehara, Z. XPS Analysis of Lithium Surfaces
Following Immersion in Various Solvents Containing $LiBF_4$. *J. Electrochem. Soc.* **1995**, *142*
(2), 340–347. https://doi.org/10.1149/1.2044000.

(40)   Bodenes, L.; Dedryvère, R.; Martinez, H.; Fischer, F.; Tessier, C.; Pérès, J.-P. Lithium-Ion
Batteries Working at 85°C: Aging Phenomena and Electrode/Electrolyte Interfaces Studied by
XPS. *J. Electrochem. Soc.* **2012**, *159* (10), A1739–A1746. https://doi.org/10.1149/2.061210jes.

(41)   Kosova, N. V.; Devyatkina, E. T.; Kaichev, V. V. Optimization of Ni^{2+}/Ni^{3+} Ratio in Layered
$Li(Ni,Mn,Co)O_2$ Cathodes for Better Electrochemistry. *J. Power Sources* **2007**, *174* (2), 965–
969. https://doi.org/10.1016/j.jpowsour.2007.06.051.

(42)   Glass, A. M.; Nassau, K.; Negran, T. J. Ionic Conductivity of Quenched Alkali Niobate and
Tantalate Glasses. *J. Appl. Phys.* **1978**, *49* (9), 4808–4811. https://doi.org/10.1063/1.325509.

(43)   Özer, N.; Lampert, C. M. Electrochemical Lithium Insertion in Sol-Gel Deposited $LiNbO_3$
Films. *Sol. Energy Mater. Sol. Cells* **1995**, *39* (2–4), 367–375. https://doi.org/10.1016/0927-
0248(96)80002-X.

(44)   Xiao, Y.; Miara, L. J.; Wang, Y.; Ceder, G. Computational Screening of Cathode Coatings for
Solid-State Batteries. *Joule* **2019**, *3* (5), 1252–1275.
https://doi.org/10.1016/j.joule.2019.02.006.

(45)   Nolan, A. M.; Liu, Y.; Mo, Y. Solid-State Chemistries Stable with High-Energy Cathodes for
Lithium-Ion Batteries. *ACS Energy Lett.* **2019**, *4* (10), 2444–2451.
https://doi.org/10.1021/acsenergylett.9b01703.

(46)   Auvergniot, J.; Cassel, A.; Foix, D.; Viallet, V.; Seznec, V.; Dedryvère, R. Redox Activity of
Argyrodite Li_6PS_5Cl Electrolyte in All-Solid-State Li-Ion Battery: An XPS Study. *Solid State
Ionics* **2017**, *300*, 78–85. https://doi.org/10.1016/j.ssi.2016.11.029.

(47)   Auvergniot, J.; Cassel, A.; Ledeuil, J. B.; Viallet, V.; Seznec, V.; Dedryvère, R. Interface
Stability of Argyrodite Li_6PS_5Cl toward $LiCoO_2$, $LiNi_{1/3}Co_{1/3}Mn_{1/3}O_2$, and $LiMn_2O_4$ in Bulk
All-Solid-State Batteries. *Chem. Mater.* **2017**, *29* (9), 3883–3890.
https://doi.org/10.1021/acs.chemmater.6b04990.

(48)   Koerver, R.; Walther, F.; Aygün, I.; Sann, J.; Dietrich, C.; Zeier, W. G.; Janek, J. Redox-Active
Cathode Interphases in Solid-State Batteries. *J. Mater. Chem. A* **2017**, *5* (43), 22750–22760.
https://doi.org/10.1039/C7TA07641J.

(49)   Koerver, R.; Aygün, I.; Leichtweiß, T.; Dietrich, C.; Zhang, W.; Binder, J. O.; Hartmann, P.;
Zeier, W. G.; Janek, J. Capacity Fade in Solid-State Batteries: Interphase Formation and
Chemomechanical Processes in Nickel-Rich Layered Oxide Cathodes and Lithium

Thiophosphate Solid Electrolytes. *Chem. Mater.* **2017**, *29* (13), 5574–5582. https://doi.org/10.1021/acs.chemmater.7b00931.

(50)   Nagai, E.; Arthur, T. S.; Bonnick, P.; Suto, K.; Muldoon, J. The Discharge Mechanism for Solid-State Lithium-Sulfur Batteries. *MRS Adv.* **2019**, *4* (49), 2627–2634. https://doi.org/10.1557/adv.2019.255.

(51)   Wang, Y.; Matsuyama, T.; Deguchi, M.; Hayashi, A.; Nakao, A.; Tatsumisago, M. X-Ray Photoelectron Spectroscopy for Sulfide Glass Electrolytes in the Systems Li_2S–P_2S_5 and Li_2S–P_2S_5–LiBr. *J. Ceram. Soc. Japan* **2016**, *124* (5), 597–601. https://doi.org/10.2109/jcersj2.16006.

(52)   Dietrich, C.; Koerver, R.; Gaultois, M. W.; Kieslich, G.; Cibin, G.; Janek, J.; Zeier, W. G. Spectroscopic Characterization of Lithium Thiophosphates by XPS and XAS – a Model to Help Monitor Interfacial Reactions in All-Solid-State Batteries. *Phys. Chem. Chem. Phys.* **2018**, *20* (30), 20088–20095. https://doi.org/10.1039/C8CP01968A.

(53)   Tan, D. H. S.; Wu, E. A.; Nguyen, H.; Chen, Z.; Marple, M. A. T.; Doux, J.; Wang, X.; Yang, H.; Banerjee, A.; Meng, Y. S. Elucidating Reversible Electrochemical Redox of Li_6PS_5Cl Solid Electrolyte. *ACS Energy Lett.* **2019**, *4* (10), 2418–2427. https://doi.org/10.1021/acsenergylett.9b01693.

(54)   Appapillai, A. T.; Mansour, A. N.; Cho, J.; Shao-Horn, Y. Microstructure of $LiCoO_2$ with and without "$AlPO_4$" Nanoparticle Coating: Combined STEM and XPS Studies. *Chem. Mater.* **2007**, *19* (23), 5748–5757. https://doi.org/10.1021/cm0715390.

(55)   Wang, B.; Liu, J.; Sun, Q.; Li, R.; Sham, T.-K.; Sun, X. Atomic Layer Deposition of Lithium Phosphates as Solid-State Electrolytes for All-Solid-State Microbatteries. *Nanotechnology* **2014**, *25* (50), 504007. https://doi.org/10.1088/0957-4484/25/50/504007.

(56)   Franke, R.; Chassé, T.; Streubel, P.; Meisel, A. Data Bank - Auger Parameters and Relaxation Energies of Phosphorus in Solid Compounds. *J. Electron Spectros. Relat. Phenomena* **1991**, *56* (4), 381–388.

(57)   Pralong, V.; Reddy, M. A.; Caignaert, V.; Malo, S.; Lebedev, O. I.; Varadaraju, U. V.; Raveau, B. A New Form of $LiNbO_3$ with a Lamellar Structure Showing Reversible Lithium Intercalation. *Chem. Mater.* **2011**, *23* (7), 1915–1922. https://doi.org/10.1021/cm1036524.

(58)   Lee, D.; Shank, J. C.; Tellekamp, M. B.; Doolittle, W. A.; Alamgir, F. M. Thin-Film Lithium Niobites and Their Chemical Properties for Lithium-Ion Storage and Diffusion. *ChemElectroChem* **2019**, *6* (19), 5109–5115. https://doi.org/10.1002/celc.201901347.

(59)   Li, W.; Hu, C.; Zhou, M.; Wang, K.; Li, H.; Cheng, S.; Jiang, K. The Electrochemical

Synthesis of LiNbO$_2$ in Molten Salts and Its Application for Lithium Ion Batteries with High Rate Capability. *Electrochim. Acta* **2016**, *189*, 231–236. https://doi.org/10.1016/j.electacta.2015.12.085.

(60)   Viet, A. Le; Reddy, M. V.; Jose, R.; Chowdari, B. V. R.; Ramakrishna, S. Nanostructured Nb$_2$O$_5$ Polymorphs by Electrospinning for Rechargeable Lithium Batteries. *J. Phys. Chem. C* **2010**, *114* (1), 664–671. https://doi.org/10.1021/jp9088589.

(61)   Wei, M.; Wei, K.; Ichihara, M.; Zhou, H. Nb$_2$O$_5$ Nanobelts: A Lithium Intercalation Host with Large Capacity and High Rate Capability. *Electrochem. commun.* **2008**, *10* (7), 980–983. https://doi.org/10.1016/j.elecom.2008.04.031.

(62)   Kumagai, N.; Koishikawa, Y.; Komaba, S.; Koshiba, N. Thermodynamics and Kinetics of Lithium Intercalation into Nb$_2$O$_5$ Electrodes for a 2 V Rechargeable Lithium Battery. *J. Electrochem. Soc.* **1999**, *146* (9), 3203–3210. https://doi.org/10.1149/1.1392455.

(63)   Tonti, D.; Pettenkofer, C.; Jaegermann, W. Origin of the Electrochemical Potential in Intercalation Electrodes: Experimental Estimation of the Electronic and Ionic Contributions for Na Intercalated into TiS$_2$. *J. Phys. Chem. B* **2004**, *108* (41), 16093–16099. https://doi.org/10.1021/jp047450o.

(64)   Hausbrand, R.; Becker, D.; Jaegermann, W. A Surface Science Approach to Cathode/Electrolyte Interfaces in Li-Ion Batteries: Contact Properties, Charge Transfer and Reactions. *Prog. Solid State Chem.* **2014**, *42* (4), 175–183. https://doi.org/10.1016/j.progsolidstchem.2014.04.010.

(65)   Schwöbel, A.; Jaegermann, W.; Hausbrand, R. Interfacial Energy Level Alignment and Energy Level Diagrams for All-Solid Li-Ion Cells: Impact of Li-Ion Transfer and Double Layer Formation. *Solid State Ionics* **2016**, *288*, 224–228. https://doi.org/10.1016/j.ssi.2015.12.029.

(66)   Cherkashinin, G.; Hausbrand, R.; Jaegermann, W. Performance of Li-Ion Batteries: Contribution of Electronic Factors to the Battery Voltage. *J. Electrochem. Soc.* **2019**, *166* (3), A5308–A5312. https://doi.org/10.1149/2.0441903jes.

(67)   Visbal, H.; Aihara, Y.; Ito, S.; Watanabe, T.; Park, Y.; Doo, S. The Effect of Diamond-like Carbon Coating on LiNi$_{0.8}$Co$_{0.15}$Al$_{0.05}$O$_2$ Particles for All Solid-State Lithium-Ion Batteries Based on Li$_2$SeP$_2$S$_5$ Glass-Ceramics. *J. Power Sources* **2016**, *314*, 85–92. https://doi.org/10.1016/j.jpowsour.2016.02.088.

(68)   Ahmed, S.; Pokle, A.; Schweidler, S.; Beyer, A.; Bianchini, M.; Walther, F.; Mazilkin, A.; Hartmann, P.; Brezesinski, T.; Janek, J.; et al. The Role of Intragranular Nanopores in Capacity Fade of Nickel-Rich Layered Li(Ni$_{1-x-y}$Co$_x$Mn$_y$)O$_2$ Cathode Materials. *ACS Nano* **2019**, *13* (9),

10694–10704. https://doi.org/10.1021/acsnano.9b05047.

(69) Heitjans, P.; Masoud, M.; Feldhoff, A.; Wilkening, M. NMR and Impedance Studies of Nanocrystalline and Amorphous Ion Conductors: Lithium Niobate as a Model System. *Faraday Discuss.* **2007**, *134*, 67–82. https://doi.org/10.1039/B602887J.

(70) Zhang, W.; Leichtweiß, T.; Culver, S. P.; Koerver, R.; Das, D.; Weber, D. A.; Zeier, W. G.; Janek, J. The Detrimental Effects of Carbon Additives in $Li_{10}GeP_2S_{12}$-Based Solid-State Batteries. *ACS Appl. Mater. Interfaces* **2017**, *9* (41), 35888–35896. https://doi.org/10.1021/acsami.7b11530.

(71) Yoon, K.; Kim, J.-J.; Seong, W. M.; Lee, M. H.; Kang, K. Investigation on the Interface between $Li_{10}GeP_2S_{12}$ Electrolyte and Carbon Conductive Agents in All-Solid-State Lithium Battery. *Sci. Rep.* **2018**, *8* (1), 1–7. https://doi.org/10.1038/s41598-018-26101-4.

(72) Deng, S.; Sun, Y.; Li, X.; Ren, Z.; Liang, J.; Doyle-Davis, K.; Liang, J.; Li, W.; Norouzi Banis, M.; Sun, Q.; et al. Eliminating the Detrimental Effects of Conductive Agents in Sulfide-Based Solid-State Batteries. *ACS Energy Lett.* **2020**, 1243–1251. https://doi.org/10.1021/acsenergylett.0c00256.

(73) Randau, S.; Walther, F.; Neumann, A.; Schneider, Y.; Negi, R. S.; Mogwitz, B.; Sann, J.; Becker-Steinberger, K.; Danner, T.; Hein, S.; et al. On the Additive Microstructure in Composite Cathodes and Alumina-Coated Carbon Microwires for Improved All-Solid-State Batteries. *Chem. Mater.* **2021**, Article ASAP. https://doi.org/10.1021/acs.chemmater.0c04454.

(74) Richards, W. D.; Miara, L. J.; Wang, Y.; Kim, J. C.; Ceder, G. Interface Stability in Solid-State Batteries. *Chem. Mater.* **2016**, *28* (1), 266–273. https://doi.org/10.1021/acs.chemmater.5b04082.

(75) Nolan, A. M.; Zhu, Y.; He, X.; Bai, Q.; Mo, Y. Computation-Accelerated Design of Materials and Interfaces for All-Solid-State Lithium-Ion Batteries. *Joule* **2018**, *2* (10), 2016–2046. https://doi.org/10.1016/j.joule.2018.08.017.

(76) Lim, C. B.; Park, Y. J. Precursor-based Surface Modification of Cathodes Using Ta and W for Sulfide-based All-solid-state Batteries. *Sci. Rep.* **2020**, *10* (1), 10501. https://doi.org/10.1038/s41598-020-67493-6.

(77) Zhang, Y.; Tian, Y.; Xiao, Y.; Miara, L. J.; Aihara, Y.; Tsujimura, T.; Shi, T.; Scott, M. C.; Ceder, G. Direct Visualization of the Interfacial Degradation of Cathode Coatings in Solid State Batteries: A Combined Experimental and Computational Study. *Adv. Energy Mater.* **2020**, *10* (27), 1903778. https://doi.org/10.1002/aenm.201903778.

(78) Bartsch, T.; Strauss, F.; Hatsukade, T.; Schiele, A.; Kim, A.-Y.; Hartmann, P.; Janek, J.;

Brezesinski, T. Gas Evolution in All-Solid-State Battery Cells. *ACS Energy Lett.* **2018**, *3*, 2539–2543. https://doi.org/10.1021/acsenergylett.8b01457.

(79)   Strauss, F.; Teo, J. H.; Schiele, A.; Bartsch, T.; Hatsukade, T.; Hartmann, P.; Janek, J.; Brezesinski, T. Gas Evolution in Lithium-Ion Batteries: Solid versus Liquid Electrolyte. *ACS Appl. Mater. Interfaces* **2020**, *12* (18), 20462–20468. https://doi.org/10.1021/acsami.0c02872.

(80)   Mahne, N.; Renfrew, S. E.; McCloskey, B. D.; Freunberger, S. A. Electrochemical Oxidation of Lithium Carbonate Generates Singlet Oxygen. *Angew. Chemie Int. Ed.* **2018**, *57* (19), 5529–5533. https://doi.org/10.1002/anie.201802277.

(81)   Hatsukade, T.; Schiele, A.; Hartmann, P.; Brezesinski, T.; Janek, J. Origin of Carbon Dioxide Evolved during Cycling of Nickel-Rich Layered NCM Cathodes. *ACS Appl. Mater. Interfaces* **2018**, *10* (45), 38892–38899. https://doi.org/10.1021/acsami.8b13158.

(82)   Wandt, J.; Freiberg, A. T. S.; Ogrodnik, A.; Gasteiger, H. A. Singlet Oxygen Evolution from Layered Transition Metal Oxide Cathode Materials and Its Implications for Lithium-Ion Batteries. *Mater. Today* **2018**, *21* (8), 825–833. https://doi.org/10.1016/j.mattod.2018.03.037.

(83)   Strauss, F.; Teo, J. H.; Maibach, J.; Kim, A.-Y.; Mazilkin, A.; Janek, J.; Brezesinski, T. Li_2ZrO_3-Coated NCM622 for Application in Inorganic Solid-State Batteries: Role of Surface Carbonates in the Cycling Performance. *ACS Appl. Mater. Interfaces* **2020**, *12* (51), 57146–57154. https://doi.org/10.1021/acsami.0c18590.

(84)   Kuwata, N.; Iwagami, N.; Matsuda, Y.; Tanji, Y.; Kawamura, J. Thin Film Batteries with Li_3PO_4 Solid Electrolyte Fabricated by Pulsed Laser Deposition. *ECS Trans.* **2019**, *16* (26), 53–60. https://doi.org/10.1149/1.3111821.

(85)   Touboul, M.; Sephar, N.; Quarton, M. Electrical Conductivity and Phase Diagram of the System Li_2SO_4-Li_3PO_4. *Solid State Ionics* **1990**, *38* (3–4), 225–229. https://doi.org/10.1016/0167-2738(90)90425-Q.

(86)   Wang, S.; Yan, M.; Li, Y.; Vinado, C.; Yang, J. Separating Electronic and Ionic Conductivity in Mix-Conducting Layered Lithium Transition-Metal Oxides. *J. Power Sources* **2018**, *393*, 75–82. https://doi.org/10.1016/j.jpowsour.2018.05.005.

(87)   Zahnow, J.; Bernges, T.; Wagner, A.; Bohn, N.; Binder, J. R.; Zeier, W. G.; Elm, M. T.; Janek, J. Impedance Analysis of NCM Cathode Materials: Electronic and Ionic Partial Conductivities and the Influence of Microstructure. *ACS Appl. Energy Mater.* **2021**, Article ASAP. https://doi.org/10.1021/acsaem.0c02606.

(88)   Hakari, T.; Deguchi, M.; Mitsuhara, K.; Ohta, T.; Saito, K.; Orikasa, Y.; Uchimoto, Y.; Kowada, Y.; Hayashi, A.; Tatsumisago, M. Structural and Electronic-State Changes of a

Sulfide Solid Electrolyte during the Li Deinsertion-Insertion Processes. *Chem. Mater.* **2017**, *29* (11), 4768–4774. https://doi.org/10.1021/acs.chemmater.7b00551.

(89)   Dissanayake, M. A. K. L.; Mellander, B.-E. Phase Diagram and Electrical Conductivity of the Li$_2$SO$_4$-Li$_2$CO$_3$ System. *Solid State Ionics* **1986**, *21* (4), 279–285. https://doi.org/10.1016/0167-2738(86)90190-6.

(90)   Homma, K.; Liu, Y.; Sumita, M.; Tamura, R.; Fushimi, N.; Iwata, J.; Tsuda, K.; Kaneta, C. Optimization of a Heterogeneous Ternary Li$_3$PO$_4$–Li$_3$BO$_3$–Li$_2$SO$_4$ Mixture for Li-Ion Conductivity by Machine Learning. *J. Phys. Chem. C* **2020**, *124* (24), 12865–12870. https://doi.org/10.1021/acs.jpcc.9b11654.

(91)   Nagao, K.; Nose, M.; Kato, A.; Sakuda, A.; Hayashi, A.; Tatsumisago, M. Preparation and Characterization of Glass Solid Electrolytes in the Pseudoternary System Li$_3$BO$_3$-Li$_2$SO$_4$-Li$_2$CO$_3$. *Solid State Ionics* **2017**, *308*, 68–76. https://doi.org/10.1016/j.ssi.2017.05.009.

(92)   Koerver, R.; Zhang, W.; de Biasi, L.; Schweidler, S.; Kondrakov, A. O.; Kolling, S.; Brezesinski, T.; Hartmann, P.; Zeier, W. G.; Janek, J. Chemo-Mechanical Expansion of Lithium Electrode Materials – on the Route to Mechanically Optimized All-Solid-State Batteries. *Energy Environ. Sci.* **2018**, *11* (8), 2142–2158. https://doi.org/10.1039/C8EE00907D.

(93)   Zhu, Y.; He, X.; Mo, Y. First Principles Study on Electrochemical and Chemical Stability of Solid Electrolyte–Electrode Interfaces in All-Solid-State Li-Ion Batteries. *J. Mater. Chem. A* **2016**, *4* (9), 3253–3266. https://doi.org/10.1039/C5TA08574H.

(94)   Shimada, S.; Kodaira, K.; Matsushita, T. A Study of the Formation of LiNbO$_3$ in the System Li$_2$CO$_3$-Nb$_2$O$_5$. *Thermochim. Acta* **1978**, *23* (1), 135–144. https://doi.org/10.1016/0040-6031(78)85119-3.

(95)   Nakamura, T.; Amezawa, K.; Kulisch, J.; Zeier, W. G.; Janek, J. Guidelines for All-Solid-State Battery Design and Electrode Buffer Layers Based on Chemical Potential Profile Calculation. *ACS Appl. Mater. Interfaces* **2019**, *11* (22), 19968–19976. https://doi.org/10.1021/acsami.9b03053.

(96)   Shi, S.; Qi, Y.; Li, H.; Hector, L. G. Defect Thermodynamics and Diffusion Mechanisms in Li$_2$CO$_3$ and Implications for the Solid Electrolyte Interphase in Li-Ion Batteries. *J. Phys. Chem. C* **2013**, *117* (17), 8579–8593. https://doi.org/10.1021/jp310591u.

Table of Contents

For Table of Contents.